

LA-UR-18-28429 (Accepted Manuscript)

Quantized Electronic Doping towards Atomically Controlled “Charge-Engineered” Semiconductor Nanocrystals

Capitani, Chiara; Crooker, Scott A.; Pinchetti, Valerio; Gariano, G.;
Santiago-Gonzalez, B.; Santambrogio, M.; Prato, M.; Brescia, R.;
Bellato, F.; Meinardi, F.; Brovelli, S.

Provided by the author(s) and the Los Alamos National Laboratory (2019-03-22).

To be published in: Nano Letters

DOI to publisher's version: 10.1021/acs.nanolett.8b04904

Permalink to record: <http://permalink.lanl.gov/object/view?what=info:lanl-repo/lareport/LA-UR-18-28429>

Disclaimer:

Approved for public release. Los Alamos National Laboratory, an affirmative action/equal opportunity employer, is operated by the Los Alamos National Security, LLC for the National Nuclear Security Administration of the U.S. Department of Energy under contract DE-AC52-06NA25396. Los Alamos National Laboratory strongly supports academic freedom and a researcher's right to publish; as an institution, however, the Laboratory does not endorse the viewpoint of a publication or guarantee its technical correctness.

Quantized Electronic Doping Towards Atomically Controlled 'Charge-Engineered' Semiconductor Nanocrystals

Chiara Capitani,^{1,2†} Valerio Pinchetti,^{1†} Graziella Gariano,² Beatriz Santiago-González,^{1,3} Carlo Santambrogio,⁴ Marcello Campione,⁵ Mirko Prato,⁶ Rosaria Brescia,⁶ Andrea Camellini,⁷ Fulvio Bellato,¹ Francesco Carulli,¹ Abhinav Anand,¹ Margherita Zavelani-Rossi,⁷ Francesco Meinardi,¹ Scott A. Crooker,^{8*} Sergio Brovelli.^{1*}

¹ Dipartimento di Scienza dei Materiali, Università degli Studi di Milano – Bicocca, Via R. Cozzi 55, I-20125, Milano, Italy;

² Glass to Power SpA, Via F. Daverio 6, I-20135, Milano, Italy;

³ International Iberian Nanotechnology Laboratory, Nanophotonics Department, Ultrafast Bio- and Nanophotonics Group, Avenida Mestre José Veiga s/n 4715-330 Braga, Portugal;

⁴ Dipartimento di Biotecnologie e Bioscienze, Università degli Studi di Milano – Bicocca, Piazza della Scienza 2, I-20126 Milano, Italy;

⁵ Dipartimento di Scienze dell'Ambiente e del Territorio e di Scienze della Terra, Università degli Studi Milano-Bicocca, Piazza della Scienza, I-20125 Milano, Italy;

⁶ Istituto Italiano di Tecnologia, Via Morego 30, 16163 Genova, Italy;

⁷ Dipartimento di Energia, Politecnico di Milano and IFN-CNR, Milano, Italy.

⁸ National High Magnetic Field Laboratory, Los Alamos National Laboratory, Los Alamos, New Mexico, 87545, United States.

[†] These authors contributed equally to this work.

'Charge engineering' of semiconductor nanocrystals (NCs) through so-called electronic impurity doping is a long-lasting challenge in colloidal chemistry and holds promise for ground-breaking advancements in many optoelectronic, photonic and spin-based nanotechnologies. To date, our knowledge is limited to a few paradigmatic studies on a small number of model compounds and doping conditions, with important electronic dopants still unexplored in nanoscale systems. Equally importantly, fine tuning of charge engineered NCs is hampered by the statistical limitations of traditional approaches. The resulting intrinsic doping inhomogeneity restricts fundamental studies to statistically averaged behaviours and complicates the realization of advanced device concepts based on their advantageous functionalities. Here we aim to address these issues by realizing the first example of II-VI NCs electronically doped with an exact number of heterovalent gold atoms, a known *p*-type acceptor impurity in bulk chalcogenides. Single-dopant accuracy across entire NC ensembles is obtained through a novel non-injection synthesis employing ligand-exchanged gold clusters as 'quantized' dopant sources to seed the nucleation of CdSe NCs in organic media. Structural, spectroscopic and magneto-optical investigations trace a comprehensive picture of the physical processes resulting from the exact doping level of the NCs. Gold atoms, doped here for the first time into II-VI NCs, are found to incorporate as nonmagnetic Au⁺ species activating intense size-tuneable intragap photoluminescence and artificially offsetting the hole occupancy of valence band states. Fundamentally, the transient conversion of Au⁺ to paramagnetic Au²⁺ (5d⁹ configuration) under optical excitation results in strong photoinduced magnetism and diluted magnetic semiconductor behaviour revealing the contribution of individual paramagnetic impurities to the macroscopic magnetism of the NCs. Altogether, our results demonstrate a new chemical approach towards NCs with physical functionalities tailored to the single impurity level and offer a versatile platform for future investigations and device exploitation of individual and collective impurity processes in quantum confined structures.

Keywords: nanocrystals, doping, diluted magnetic semiconductors, metal quantum clusters, seeded growth, photoluminescence

Colloidal semiconductor nanocrystals (NCs), owing to their size tuneable electronic properties and solution processability, have long been proposed as versatile chemically-synthesized alternatives for many photonic, optoelectronic and quantum computational technologies, as well as super-atomic functional building blocks for bottom-up assembled artificial metamaterials¹⁻⁴. Since their original discovery over thirty years ago, tremendous advancements in colloidal and surface chemistry⁵⁻⁸, NC physics and device application⁹⁻¹¹ have brought this vision closer to reality. At present, however, one challenge that remains outstanding in NCs science is so-called *charge engineering* by permanent and controlled introduction of optically and/or electrically functional charges into NCs^{13,15-18}. Charge engineering of *p*- and *n*-type bulk semiconductors through the insertion of heterovalent atoms with respect to the host lattice, commonly referred to as ‘electronic impurity doping’, is standard practice and arguably the most powerful material engineering paradigm underpinning contemporary microelectronics. Its extension to NCs synthesized directly in the liquid phase, aided by the enhanced interaction between the impurity charges and the spatially-confined carriers, would unlock fundamental properties that cannot be achieved with other motifs, such as unidirectional emission-only photophysics¹²⁻¹⁴, enhanced charge mobility¹⁵⁻¹⁸ and photo-controlled magnetic behaviours^{19, 20}. These advantageous properties make charge-engineered NCs not only interesting systems to be investigated per se, but potential cornerstones for ground-breaking advancements in applications ranging as widely as lasers²¹⁻²³, transistors^{15, 24, 25}, solar cells^{17, 26, 27}, luminescent solar concentrators^{13, 14}, plasmonic²⁸ and spintronic devices^{19, 20} fabricated via solution-based processes^{29, 30}.

Despite this promise, our knowledge of electronically doped NCs is still limited to a relatively small number of model compounds and doping conditions. For example, direct colloidal synthesis or cation exchange routes are established only for II-VI or III-V NCs doped with copper, silver, iron or indium^{15, 16, 29, 31-37}, whereas NCs doped with aluminium have been only once reported by Norris and co-workers³⁸. On the other hand, doping with an important amphoteric electronic impurity such as gold, which is a known *p*-type dopant capable of assuming +1, +3, as well as +2 oxidation states in bulk II-VI semiconductors³⁹⁻⁴⁴, has never been reported in NCs. Au-doping has been successfully obtained in InP NCs where In³⁺ cations have been substituted with Au³⁺ cations^{32, 45}.

Equally importantly, progress towards charge engineering of NCs has long been hampered by the intrinsic statistical limitations of traditional doping approaches, which operate at the ensemble level and lead to a Poissonian distribution of impurities across the NC population⁴⁶⁻⁴⁹. This has historically restricted fundamental studies to statistically averaged behaviours and has complicated in-depth investigations of the physical impact of isolated charges (so-called solotronic effects) into nanoscale hosts due to parasitic effects by doping inhomogeneity in lightly doped NCs – for example, given an average doping level of three impurities per NC, only ~20% of the NCs contain exactly three dopants

and as much as 5% of the ensemble is entirely undoped. Recently, a first step towards overcoming the ‘Poissonian bottleneck’ has been elegantly achieved by the introduction of so-called quantized or exact doping strategies⁵⁰⁻⁵³ that propose the use of size-focused metal clusters or organometallic complexes as nucleation seeds for doped NCs. Since such seeds are composed of a ‘magic number’ of atoms, these approaches enable one to achieve predetermined atomic resolution of the doping level in individual NCs and to produce homogeneously doped NC ensembles. However, quantized doping was only demonstrated using copper compounds, either in the form of chemically unstable benzenethiol complexes⁵⁴ or water-soluble clusters resulting in poor NC quality⁵¹. Crucially, no study has yet investigated the functional implications of quantized doping with electronic impurities. To date, *i*) the generalization of the strategy to electronic dopants, *ii*) its extension to organic synthesis routes enabling enhanced control over the material quality, and *iii*) the in-depth investigation of the emerging physical properties remain open challenges in NC science. The payback for such advancements will, in turn, be the long sought-after capability to generate a library of chemically synthesized nanostructures finely engineered at the single charge level.

In this work, we make significant progress in these three directions by realizing, for the first time, CdSe NCs electronically doped with gold atoms through a new quantized-doping route using magic-sized gold clusters in organic media as nucleation seeds. The obtained Au:CdSe NCs are the first example of II-VI NCs incorporating gold dopants produced by any known route. Structural and analytical characterization, combined with spectroscopic measurements and chemical etching experiments, indicate that the clusters consist of seven gold atoms and that they seed the nucleation of CdSe NC containing an equivalent number of gold impurities preferentially located in the particle core. Consistent with previous studies of bulk materials³⁹⁻⁴³, the dopants are found to incorporate as Au⁺ acceptors. In NCs, owing to the quantum confinement effect, this results in long-lived, widely Stokes-shifted luminescence, spectrally tuneable from the visible to the near infrared by control of the particle size. Photoluminescence (PL) and transient transmission (TT) experiments on Au:CdSe NCs as a function of the excitation density highlight, for the first time, the effect of nonradiative Auger relaxation processes on the photophysics of electronically-doped NCs. They also reveal the intimate link between the dopant and the intrinsic band-edge excitonic PL that is observed exclusively upon optical saturation of the Au⁺ acceptor states with valence band (VB) photoholes. Also importantly, magnetic circular dichroism (MCD) measurements reveal that the transient change of the oxidation state from Au⁺ (with nonmagnetic 5d¹⁰ electronic configuration) to Au²⁺ (with paramagnetic 5d⁹ electronic configuration) during the multistep exciton recombination process results in strong photo-induced paramagnetism. Fundamentally, such a photo-triggered diluted magnetic semiconductor (DMS) behaviour follows a step-like trend with the illumination intensity revealing

the contribution of individual paramagnetic impurities to the macroscopic magnetism of the NCs. The process is formalized through a phenomenological dynamic model, indicating that the maximum paramagnetic response is obtained when all gold impurities in the NCs are photo-converted from their native non-magnetic Au^+ state into the paramagnetic Au^{2+} configuration. Altogether, our results suggest a new chemical approach towards NCs with physical functionalities tailored to the single impurity level and demonstrates an unprecedented strategy for exquisite control of electronic impurity doping of NCs. This will provide a platform for future investigations and device exploitation of individual and collective processes in charge engineered quantum confined structures.

Synthesis of quantized doped Au:CdSe NCs. The synthesis route for quantized-doped Au:CdSe NCs is schematically depicted in **Figure 1a** and consists in a three-step procedure starting with the aqueous preparation of the Au clusters followed by phase transfer to a non-polar medium via ligand exchange and the seeded growth of Au-doped CdSe NCs through a non-injection route. First, monodisperse clusters were obtained by direct reduction of HAuCl_4 (0.02 M) using L-glutathione (GSH, 0.1 M) that also acts as a capping ligand⁵⁵. After 24 hours of vigorous stirring at 70°C, the clusters were purified by adding isopropanol to the solution (1:2 volume ratio) and centrifuged at 6500 rpm for 20 minutes. This procedure was repeated thrice and the purified clusters were then dispersed in ultrapure water. Before proceeding with the synthesis of the doped CdSe NCs, we characterized the clusters both for their core size and for the composition of their ligand shell by electrospray ionization mass spectrometry (ESI-MS), optical absorption, and X-ray photoelectron spectroscopy (XPS). The ESI-MS data collected in positive-ion mode shown in **Figure 1b** and in the Supporting Information (**Figure S1** and **Table S1**) indicate that the cluster population is nearly monodisperse and consists of systems composed of seven gold atoms capped by three GSH molecules. This is confirmed by the perfect agreement between the simulated isotopic distribution patterns and the respective experimental ESI-MS spectra and by the optical absorption spectrum in **Figure 1c** showing a first absorption feature at ~ 2.9 eV corresponding to the energy gap of Au_7 clusters predicted by the jellium model (~ 2.89 eV)^{56, 57}. The XPS spectrum of the clusters in **Figure 1d** shows the typical $4f_{7/2}$ and $4f_{5/2}$ doublet of gold at 84.3 eV and 88 eV, both slightly shifted with respect to the binding energy of metallic gold (84.0 eV, 87.7 eV)^{58, 59}. The fit of the XPS spectrum reveals that Au(0) accounts for 27% of total gold atoms while 73% of the atoms are in Au(I) state, corresponding to 2 Au(0) and 5 Au(I) atoms per Au_7 cluster. Once the Au_7 -GSH clusters have been structurally characterized, we proceeded with the ligand exchange reaction with 1-dodecanethiol (DDT) that renders them compatible with the seeding reaction of CdSe NCs. To achieve this goal, the aqueous solution of Au_7 -GSH clusters was first adjusted to pH \sim 9.0 by adding NaOH 1 M dropwise. Then, 5 mL of Au_7 -GSH basic solution (76 μM) was destabilized with 5 mL of

tetraoctylammonium bromide (TOABr.) in ethanol (0.02 M). After 2 minutes of vigorous stirring, 5 mL of DDT (0.15 M) in toluene were finally added. The reaction mixture was then heated to 70°C and kept under vigorous stirring to promote the phase transfer. After 1 hour, the toluene phase was separated and washed thrice with ultrapure water to remove water-soluble impurities. Importantly, the ligand exchange procedure does not alter the size of the metallic core, as highlighted by the optical absorption spectrum of the DDT-capped Au clusters that resembles perfectly that of the Au₇-GSH analogues (**Figure 1c**). We notice that, due to difficulties in sample ionization, ESI-MS measurements are inconclusive for the DDT capped clusters. XPS measurements on DDT-capped Au₇ clusters shown in **Figure 1d** highlight the presence of nearly exclusively Au(I) species, suggesting effective coordination of gold atoms by the DDT ligands. As a final step of the synthesis route, the Au₇-DDT clusters were introduced as nucleation seeds in the non-injection growth of CdSe NCs⁶⁰. Undoped reference NCs were first produced to optimize the reaction parameters and to estimate the concentration of the Au₇-DDT cluster required for seeding a monodisperse ensemble of Au:CdSe NCs. Here, selenium powder (0.05 mmol), and cadmium myristate (0.1 mmol) were added into a three-neck flask with 6.38 mL of 1-octadecene and 1 mL of oleic acid (OA). To synthesize doped NCs, 2.5 mL of Au₇-DDT (76 μM) were added to the reaction mixture. The mixture was degassed for 15 minutes in vacuum at room temperature and successively stirred and heated to 210°C for 1 hour under nitrogen flow. The samples were finally purified twice with hexane/ethanol co-solvents by centrifugation (4500 rpm, 10 min) to remove excess ligands and unreacted clusters. Importantly, in the cluster-seeded reaction, nucleation of doped CdSe NCs is observed at significantly lower temperature (~170°C, Supporting **Figure S2**) with respect to the undoped counterparts (~210°C), confirming that the gold clusters act as preferential nucleation seeds for CdSe NCs. As discussed below, in the presence of excess cluster seeds, such an effect further hinders the homonucleation of undoped CdSe particles leading to homogeneously doped Au:CdSe NCs ensembles. Representative transmission electron microscopy (TEM) image and size distribution statistics of the doped NCs are reported in **Figure 1e** and Supporting **Figure S3** showing spherical particles with average radius $R=1.65\pm 0.2$ nm, as confirmed by the optical absorption data reported below. Inductively coupled plasma atomic emission spectroscopy (ICP-AES) analysis indicates that the atomic percentage of gold in these NCs is 0.8 at%, corresponding, as we demonstrate below, to seven Au atoms per NC. In **Figure 1f**, we compare the XRD pattern of doped and undoped NCs of analogous size and of bulk CdSe in zincblende (ZB) crystal structure. The same cubic structure is observed for all systems indicating that the cluster seeding process does not affect the final crystal structure of the host NCs. No diffraction signal due to gold nanoparticles is observed for the doped NCs sample, indicating that Au nanoparticles do not nucleate during the growth of the Au:CdSe NCs.

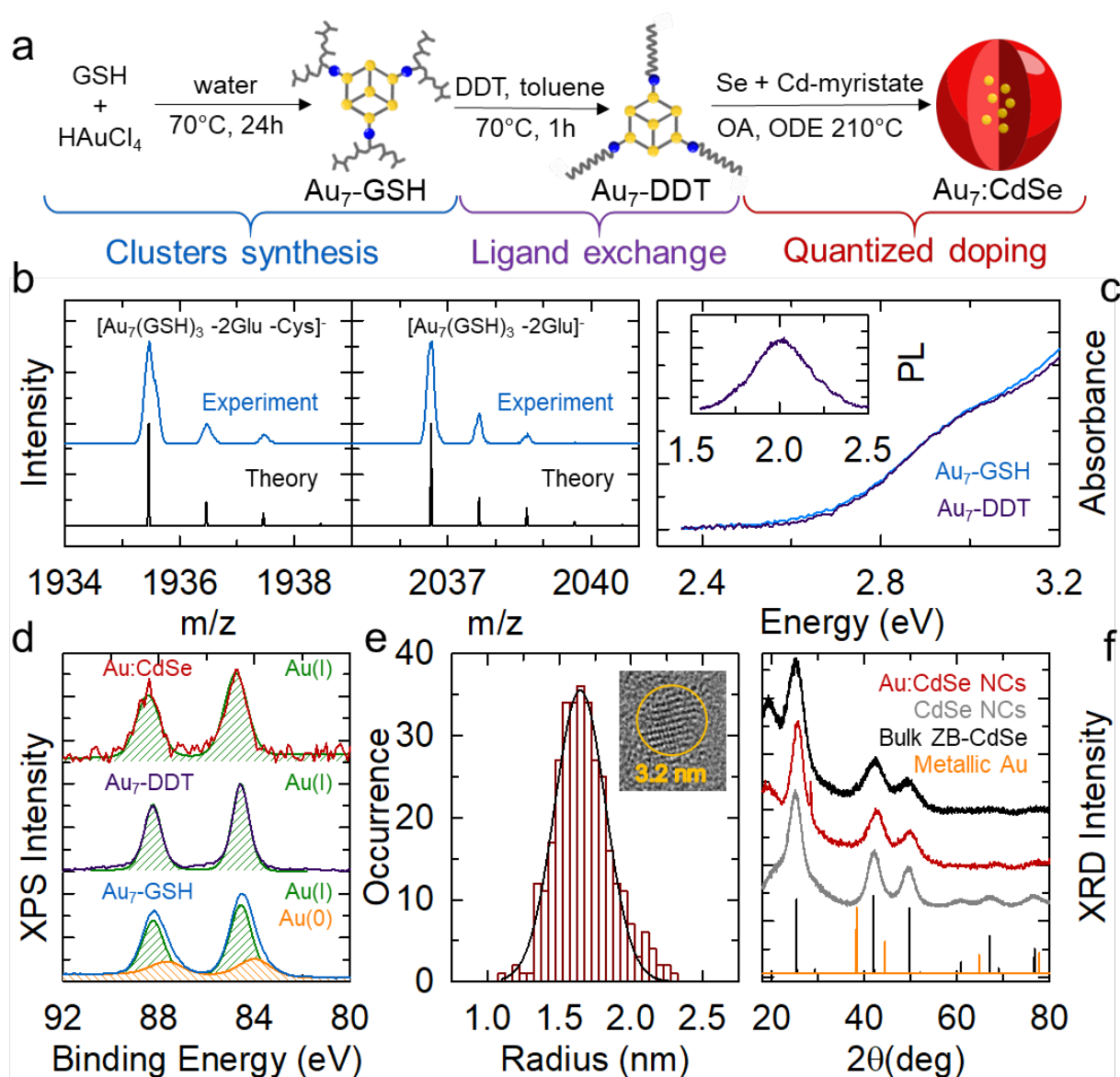


Figure 1. Synthesis and characterization of Au₇-clusters and Au:CdSe NCs. (a) Schematics of the three-step synthesis strategy of quantized-doped Au:CdSe NCs. First, water-soluble Au₇-clusters were synthesized by chemical reduction of the metal precursor HAuCl₄ using glutathione (GSH), which also acts as capping ligand. Secondly, the clusters were phase-transferred from water to toluene by exchanging strongly polar GSH molecules with nonpolar 1-dodecanethiol (DDT) molecules. Finally, Au:CdSe NCs were seeded-grown using the Au₇ clusters. The depicted structure of the gold cluster is purely indicative, details of possible conformations of Au₇ clusters are found in ref.^{61, 62}. (b) Representative peaks extracted from the ESI-MS spectrum of the Au₇-GSH clusters in water indicating [Au₇(GSH)₃-2Glu-Cys]⁻ (left) and [Au₇(GSH)₃-2Glu]⁻ (right) adducts. The respective simulated isotopic patterns are reported showing close agreement with the experiment. The full spectrum with the assignment of all ESI-MS peaks is reported in the Supporting Information. (c) Optical absorption spectra of GSH- and DDT-capped Au₇ clusters (blue and purple lines, respectively) showing invariance of the metallic core upon ligand exchange. Inset: PL spectrum of Au₇-DDT clusters in toluene under 3.1 eV excitation. (d) XPS spectra for Au₇-GSH clusters (blue line) and Au:CdSe NCs (red line). Both samples show the characteristic doublet of gold 4f orbitals. For the Au₇-GSH clusters, the fit highlights both Au(0) (orange line) and Au(I) components (green line). The Au:CdSe NCs show exclusively Au(I) species (green line). (e) Size distribution and high-resolution TEM images of representative Au:CdSe NCs indicating an mean particle radius $\langle R \rangle = 1.65 \pm 0.2$ nm. The Gaussian fit to the experimental data is shown as a black line. (f) XRD pattern of undoped and Au-doped CdSe NCs (two sizes) indicating a zincblende crystal structure in all cases. The XRD pattern of bulk CdSe and metallic Au are shown as a black and orange lines respectively for references.

Optical properties of Au:CdSe NCs and analytical assessment of the quantized-doping mechanism.

Optical spectroscopy measurements provide an independent proof of the seeding effect by the Au₇-DDT clusters resulting in homogeneously quantized-doped ensembles of Au:CdSe NCs each containing the gold atomic equivalent of one Au₇ cluster seed. Importantly, they also demonstrate the incorporation of gold atoms as acceptor electronic dopants in the NCs and clarify their key role in the recombination process of BE excitons. In **Figure 2a** we show the absorption and PL spectra of representative undoped and Au-doped CdSe NCs after 1 hour of reaction time. The spectra for aliquots collected during the particle growth are reported in Supporting **Figure S4**.

The absorption spectra of both doped and undoped NCs show a 1S peak at ~2.23 eV, in agreement with $R \sim 1.6 \text{ nm}^{63}$ extracted by the TEM images. Similar to previously reported NCs doped with group 11 metals, the absorption spectrum of the Au:CdSe NCs is broader than the undoped analogues possibly due to some local structural disorder in the doped systems⁶⁴. More importantly, stark differences are observed between the emission spectra and decay dynamics of the doped and undoped NCs due to the participation of the Au⁺ impurities in the exciton recombination process. Specifically, the undoped NCs show the typical narrowband excitonic photoluminescence (BE-PL) at 2.17 eV, nearly resonant with the respective 1S absorption peak, with PL quantum yield $\Phi_{\text{PL}} = 35 \pm 4\%$. The corresponding PL decay curve shown in **Figure 2b** is slightly multi-exponential, as commonly observed for unshelled CdSe NCs, with effective exciton lifetime $\langle \tau_{\text{BE}} \rangle \sim 15 \text{ ns}$ (as extracted when the emission intensity is reduced by a factor $1/e$). In contrast, the Au:CdSe NCs exhibit exclusively a broad (FWHM=340 meV) near-infrared emission centred at 1.6 eV (hereafter indicated as Au-PL), Stokes-shifted from the respective absorption peak by $\Delta_S = 600 \text{ meV}$. The effective emission lifetime is $\langle \tau_{\text{Au-PL}} \rangle \sim 290 \text{ ns}$, around twenty-fold longer than the intrinsic exciton lifetime (**Figure 2b**). The PL efficiency is found to be $\Phi_{\text{PL}} = 13 \pm 2\%$. The spectral and dynamical behaviours of the Au:CdSe NCs are in full agreement with the Au-mediated recombination process observed in gold-doped II-VI bulk chalcogenides, where the full *d*-shell of the Au impurity gives rise to a deep acceptor level in the host forbidden gap^{39-44, 65-67}, which participates in the recombination process of BE excitons following the scheme depicted in the inset of **Figure 2a**. Specifically, following NC excitation (Step 1), the photo-hole in the NC valence band (VB) is rapidly captured by Au⁺ which temporarily changes its oxidation state to Au²⁺ (Step 2), thereby becoming optically-active for the subsequent radiative recombination of a conduction band (CB) electron (Step 3)^{39, 41-44, 66-69}. Spectro-electrochemical measurements in **Figure 2c** support this picture, showing that the Au-PL intensity increases under negative electrochemical potentials ($V_{\text{EC}} < 0 \text{ V}$). In such conditions, which correspond to raising the NC Fermi energy (central scheme in **Figure 2c**), electron traps due to dangling bonds on the NC surfaces, are progressively passivated, which suppresses nonradiative trapping of photogenerated CB electrons.

Concomitantly, excess electrons accumulating in surface defects become efficient traps for VB photoholes. On the other hand, the application of positive V_{EC} depletes surface states of electrons, activating electron traps and passivating hole traps (rightmost scheme in **Figure 2c**).

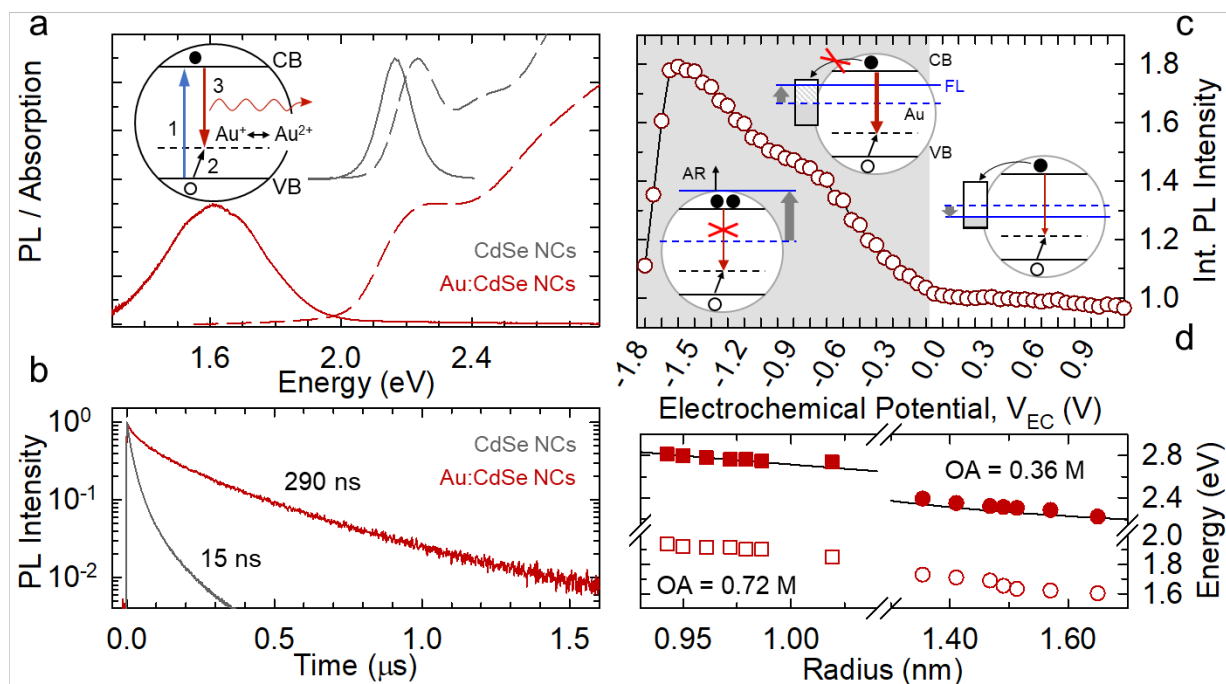


Figure 2. (a) Optical absorption (dashed lines) and PL (continuous lines) spectra of undoped (grey) and Au-doped CdSe NCs (red) in toluene (excitation energy $E_{EX}=3.1$ eV). (b) PL decay traces of bare CdSe NCs (grey) and Au: CdSe NCs (red) in toluene under 3.1 eV excitation at room temperature with a pulse frequency of 200 kHz. (c) Integrated PL intensity of Au: CdSe NCs under applied electrochemical potential (V_{EC}). Negative V_{EC} -values (shaded in grey) lead to filling of electron traps likely localized on the NCs surfaces resulting in PL brightening (central scheme). Under positive V_{EC} that depletes electron-rich traps (rightmost scheme), the PL intensity is nearly constant, pointing to a situation in which trap states are positioned in energy just above the Fermi level (FL). For $V_{EC}<-1.5$ V, the Au-PL intensity drops due to nonradiative Auger decay of negative trions (leftmost scheme). (d) Spectral positions of the 1S absorption feature – together with the predicted trend with the NC size based on ref.⁶³ (black line) – and the Au-related PL band (open symbols) as a function of particle radius for two sets of Au: CdSe NCs synthesized in the exact same conditions except for the amount of OA.

We notice that the spectro-electrochemical response is fully reproducible for many cycles (see Supporting **Figure S5**), indicating that NC surfaces are not damaged during the experiment. The $\sim 70\%$ brightening for $V_{EC}<0$ V, with no modification of the PL dynamics (Supporting **Figure S6**), together with the essentially constant PL intensity for $V_{EC}>0$ V indicate that the PL intensity is mostly limited by electron trapping occurring on a faster timescale than radiative decay, whereas hole trapping is essentially negligible. This suggests that, similar to what is observed in ternary $CuInS_2$ and lead halide perovskite NCs^{51, 70}, surface trap states are mostly positioned in energy above the Fermi level of the NC, that is, they are nearly devoided of electrons already at $V_{EC}=0$ V and thus essentially unaffected by oxidative electrochemical potentials. In addition to probing the effects of surface states, spectro-electrochemistry experiments provide a first insight into the photophysics of charged Au: CdSe NCs. Looking at the traces for $V_{EC}<-1.5$ V, we observe that the Au-PL intensity undergoes a sudden $\sim 50\%$ drop with no changes in its time dynamics (Supporting **Figure S6**). The

effect is fully reversible for many cycles (Supporting **Figure S5**) and is ascribed to efficient nonradiative Auger decay of negative trions formed by direct injection of electrons in the CB of the NCs (leftmost scheme in **Figure 2c**)^{51, 71, 72}. Transient transmission measurements as a function of the excitation fluence, discussed later in this work, corroborate this picture, showing an Auger-dominated biexciton lifetime of ~ 10 ps, consistently with Auger relaxation of negative trions occurring on a timescale faster than the time resolution of our spectro-electrochemistry setup (~ 1.5 ns), even considering a strong asymmetry between the contributions by the negative and the positive trion pathways to the biexciton Auger decay^{73, 74}. Importantly, since the Au^+ acceptor state is pinned to the host valence band^{34, 36-39, 56-59}, the dopant-mediated emission is tuneable by control of the particle size, whereas the Stokes shift is essentially independent of quantum confinement. The spectral tunability from the visible to the near IR regions achievable by doping CdSe NCs with gold is emphasized in **Figure 2d** and Supporting **Figure S7**, where we report the energy position of the 1S absorption peak and of the Au-PL for two sets of Au:CdSe NCs ranging different particle size regimes (~ 0.9 - 1.05 nm and ~ 1.35 - 1.65 nm) controlled by the amount of OA ligands used in the synthesis⁷⁵. The XPS analysis of the Au:CdSe NCs in **Figure 1d** corroborates this picture by showing the Au- $4f_{7/2}$ and Au- $4f_{5/2}$ signals respectively at 84.7 eV and 88.4 eV. Accordingly, the spectrum is well fitted by using exclusively the characteristic peaks of Au(I). Both peaks are shifted to higher energies with respect to the cluster seeds, in agreement with the acceptor role of the Au dopants in +1 oxidation state. Crucially, the absence of residual BE-PL in the emission spectrum of any Au:CdSe NCs aliquot extracted at the various stages of the particle growth (**Figure 2a** and Supporting **Figure S4**) indicates that the NC ensemble is composed solely of doped NCs. Based on this evidence, we combined structural and spectroscopic experiments with chemical microanalysis to demonstrate that, independent of the host size, each CdSe NC contains the atomic equivalent of one Au_7 cluster. In **Figure 3a** we report the Au atomic concentration (indicated as the ‘doping level’) measured by ICP-AES analysis on Au:CdSe NC with increasing size synthesized using the same Au_7 -DDT seeds (see Supporting **Table S2** for details and Supporting **Figures S8** and **S9** for the corresponding TEM images and their statistical analysis). For these measurements, the samples were purified by centrifugation and re-dispersion multiple times in order to remove any possible trace of residual unreacted clusters. According to the progressively larger volume of the NC host, the per-particle Au atomic percentage decreases with the NC radius. Most importantly, considering the size and the cubic lattice of the NC hosts (see Supporting Discussion for details), the measured doping level of each sample corresponds, within the experimental error, to seven gold atoms per particle, thus indicating that each Au_7 -DDT cluster seeds the nucleation of one quantized-doped Au:CdSe NC. Definitive confirmation of this effect is provided by optically monitoring the growth of two sets of Au:CdSe

NCs produced in the exact same synthetic conditions and differing from each other only by the concentration of the Au₇-DDT seeds. As shown in Supporting **Figure S10** and quantified in **Figure 3b**, when a 76 μM solution of cluster seeds is used, the emission spectrum of the NCs shows exclusively the Au-PL at all stages of the particle growth, indicating no nucleation of undoped CdSe NCs.

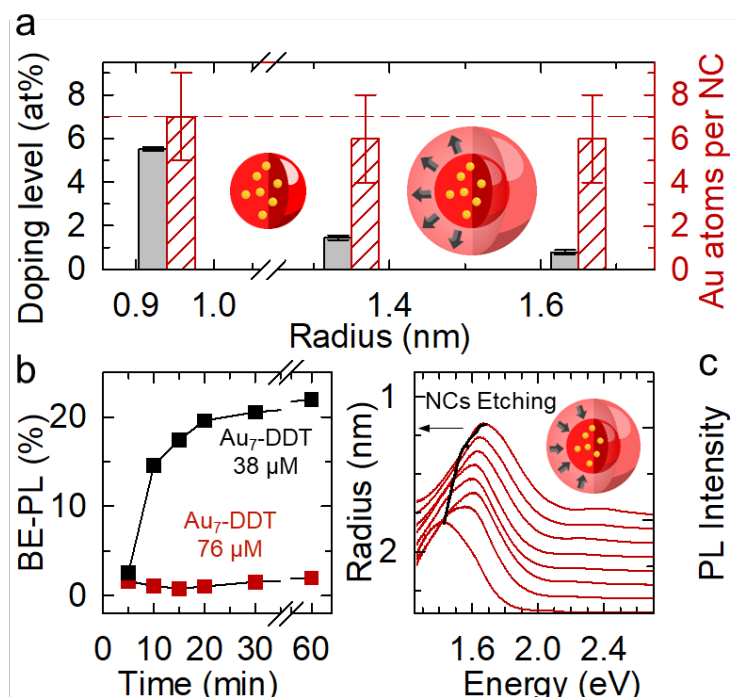


Figure 3. (a) The average NC doping level estimated by ICP-AES as a function of the particle radius. Au atomic content of doped NCs extracted by combining the spectroscopic, structural and the elemental analysis data. (b) Integrated BE-PL intensity for CdSe NCs grown with different amounts of Au₇-DDT cluster seeds, highlighting that when an excess concentration of seeds is employed, only doped particles are obtained (the BE-PL intensity is indistinguishable from the background). Hetero-nucleation of undoped CdSe NCs is observed upon lowering the concentration of seeds, thus confirming the seeding role of the gold clusters. (c) PL spectra of Au: CdSe NCs during surface etching experiments with OA (initial NC radius $R=1.81$ nm, $E_{EX}=3.1$ eV, fluence $0.3 \mu\text{J}/\text{cm}^2$), showing progressive blue shift due to enhanced quantum confinement and no measurable emergence of BE-PL, indicating that most of the Au impurities are embedded in the NC interior. The spectra are offset for clarity. The black line represents the evolution of the NC size following the etching treatment extracted following ref. ⁶³.

In contrast, when the cluster concentration is lowered to 38 μM, only the first aliquot (corresponding to 5 minutes' reaction time) shows nearly negligible BE-PL, confirming the preferential nucleation of doped particles on the cluster seeds. However, as the concentration of unreacted cluster seeds drops over time, the BE-PL rapidly intensifies indicating the development of a subpopulation of undoped NCs in the ensemble. The seeding effect by the Au₇-DDT clusters acting as exact predetermined sources of impurities for individual Au: CdSe NC, leads to the relevant conclusion that through the quantized doping approach it is possible to tune the effective doping volume concentration of entire NC ensembles by simply controlling the particle size without affecting the doping homogeneity. It is also noteworthy that the quantized-doping approach enables us to introduce Au impurities markedly more effectively than through the direct addition of molecular gold precursors to the reaction medium.

This is shown in Supporting **Figure S11**, where we report the optical spectra of CdSe NCs grown in the same synthetic conditions as our quantized-doped NCs, but using Au(I) chloride or Au acetate as dopant sources. In both cases, only the BE-PL is observed by using precursor concentrations as high as 5 wt% and partial doping of the ensemble is found by employing concentrations of 20 wt%, corresponding to fifty times the amount of gold provided by the Au₇-DDT clusters.

We finally highlight that, as a result of the seeded growth reaction, the dopants in our Au:CdSe NCs are initially located in the inner core of the host particles and the chemical microanalysis in **Figure 3a** indicates that their total number is retained also in the largest NCs. Nevertheless, it is instructive to investigate whether during particle growth the Au⁺ ions remain in the interior or diffuse towards the NC surfaces, as this could affect their physical interaction with the host carriers and ultimately the NC functionality. In order to probe this aspect, we chemically etched our NCs using OA^{38, 76}. In the case of surface segregation of dopants, chemical removal of the outer NC layers is expected to give rise to a subpopulation of undoped NCs that would be spectroscopically evident by the emergence of the BE-PL at the expense of the Au-PL intensity. Importantly, despite the NC size being reduced by nearly half (from 1.8 to 1.1 nm as extracted from the 1S energy⁶³, **Figure 3c** and Supporting **Figure S12**) and the fact that the BE emission in undoped NCs has nearly thrice the Φ_{PL} than the dopant-related PL of Au:CdSe NCs, no significant BE-PL is detected at any stage of the etching treatment and the only observed effect is the blue-shift of the Au-PL due to enhanced quantum confinement in smaller (etched) particles. These results suggest that most dopants are located in the interior also for relatively large CdSe NCs. Nevertheless, since the PL measurements are conducted in the single exciton regime, we do not rule out the possibility that some dopants might be removed from the NC during surface etching. As a result, most, if not all, of the seven Au impurities are, in principle, expected to participate in the physics of the NC hosts.

A first glimpse of this effect is provided by the evolution of the emission spectrum of the Au:CdSe NCs (R=1.65 nm) with increasing excitation power density. As shown by the PL spectra vs. average exciton occupancy ($\langle N \rangle = \sigma \times f$, where f is the excitation fluence in photons/cm² and $\sigma_{3.49\text{eV}} = 1.55 \times 10^{-15} \text{ cm}^2$ is the absorption cross section at the excitation energy of 3.49 eV)⁶³ in **Figure 4a** and quantified in terms of the integrated PL intensity in **Figure 4b**, for $\langle N \rangle$ less than ~ 1 , the NCs exhibit exclusively the broad Au-PL band at $\sim 1.45 \text{ eV}$ growing slightly sub-linearly with the excitation fluence. For larger $\langle N \rangle$ -values, the Au-PL saturates at an essentially constant intensity. This is ascribed to the activation of nonradiative Auger recombination of multi-excitons, as confirmed by TT experiments highlighting the development of a sub-nanosecond component in the 1S bleaching dynamics at increasing excitation fluence for $\langle N \rangle \geq 1$ (**Figure 4c** and Supporting **Figures S13 and S14**).

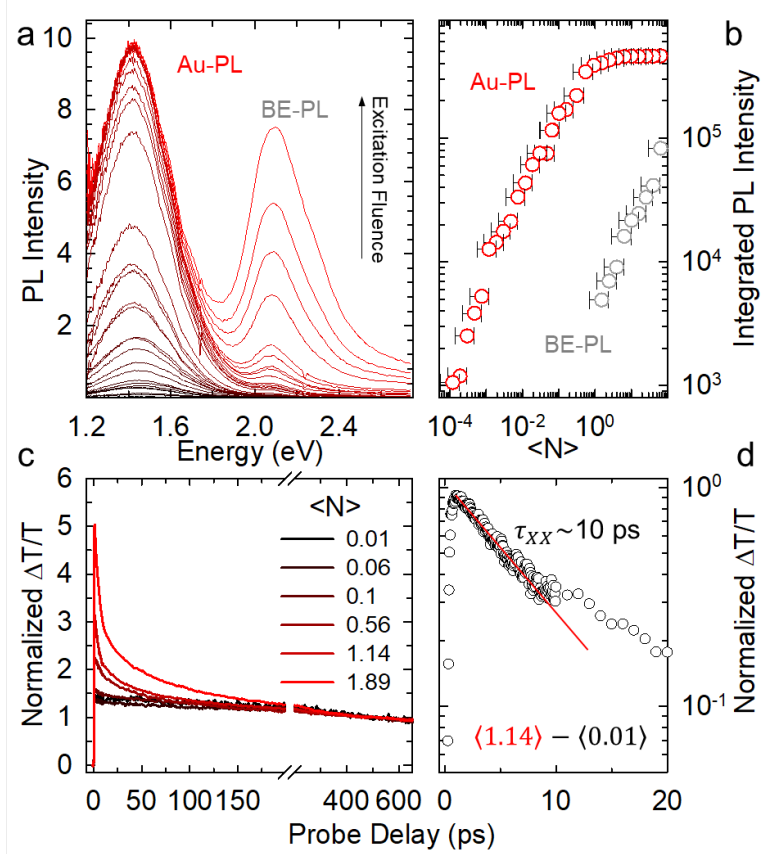


Figure 4. (a) PL spectra of Au: CdSe NCs ($R=1.81$ nm) as a function of the excitation fluence ($E_{EX}=3.5$ eV, from $4 \mu\text{J}/\text{cm}^2$ to $26 \text{ mJ}/\text{cm}^2$ as indicated by the arrow), showing saturation of the Au-PL band and the emergence of BE-PL at high fluence values. (b) Integrated PL intensity of the Au-PL (red circles) and BE-PL (grey circles) extracted from the spectra in panel ‘a’ as a function of the average NC exciton occupancy $\langle N \rangle$. The error bars represent uncertainties on the dimensions of the excitation spot and the spread in the reported cross section values for CdSe NCs^{63, 77}. (c) Photo-bleaching dynamics of Au: CdSe NCs normalized when the pump-probe delay is 600 ps at the 1S energy for increasingly higher pump fluence corresponding to the displayed average exciton occupancy $\langle N \rangle$. (d) Dynamics of bi-excitons (circles) extracted by subtracting the TT trace for $\langle N \rangle=0.01$ from the trace at $\langle M \rangle=1.14$. The fit to a single exponential decay is shown as a solid red line. The obtained biexciton lifetime is $\tau_{XX} \sim 10$ ps. All measurements were carried out at room temperature.

The analysis of the 1S bleaching time trace for $\langle N \rangle=1$ following the procedure in ref.⁷⁸, yields a biexciton lifetime $\tau_{XX}=10$ ps, in nearly perfect agreement with previous reports on undoped CdSe NCs of comparable size ($R=1.1$ nm, **Figure 4d**)⁷⁸. Invariant Auger recombination rates upon n -type doping of InAs NCs with electron donor Cu^+ ions have been reported by Yang *et al.* through transient transmission measurements.⁷⁹ In our case, however, such a behaviour is somehow surprising since, in undoped CdSe NCs, the Auger recombination of bi-excitons occurs predominantly by the so-called positive trion pathway⁷⁴, where the energy of one exciton is non-radiatively transferred to a spectator excited hole. In Au-doped NCs, Au^+ dopants behave as hole acceptors depleting the VB from photoholes, therefore, based on the similarity between our Au-doped and undoped CdSe NCs, we speculate that either the Auger process involves the holes localized in the Au^{2+} centres, which will then give no further contribution to the Au-PL, or that Auger decay takes place before hole capture by the dopants. A recent study on heavily-doped CdSe NCs indicates that capture of the photohole

by Ag^+ acceptors occurs in less than 2 ps²⁰, seemingly supporting the first interpretation that will be investigated in depth in a dedicated study. We notice that, in the nearly CW excitation conditions (excitation pulse length ~ 5 ns) used in our PL vs. fluence experiments (**Figure 4a-b**), the observed efficient Auger recombination of multiexcitons might alter the estimate of the average exciton population per NC from the nominal $\langle N \rangle$ -values, due to ultrafast nonradiative relaxation during the excitation pulse. As anticipated above, the plateauing trend of the Au-PL is accompanied by the sudden emergence and intensification of the BE-PL peak at 2.12 eV, suggesting that radiative recombination of BE excitons is activated by the optical saturation of the Au^+ acceptor states with photoholes that offsets the VB hole occupancy. Thus, the BE-PL appears for nominal $\langle N \rangle$ -values consistent, within the experimental error, with the quantized doping status of the NCs. In agreement with the above mentioned effect of Auger decay on the estimate of $\langle N \rangle$, the BE-PL shows no saturation with increasing excitation fluence and the biexciton spectral contribution to the high-energy shoulder of the BE-PL peak appears for nominal $\langle N \rangle$ -values as high as ~ 10 excitons per NC (Supporting **Figure S15**). Details of the multi-excitonic processes and dynamics in Au:CdSe NCs are beyond the scope of this work and will be treated in a separate study.

Photo-triggered magnetism of Au-doped CdSe NCs. In addition to activating new light emission properties in CdSe NCs, quantized electronic doping by Au^+ introduces important magnetic functionalities not present in undoped systems⁸⁰, conferring to Au:CdSe NCs photo-triggered paramagnetic behaviour with amplitude and dynamics directly linked to the doping level and to the Au^+ -mediated exciton recombination mechanism described in **Figure 2**. Specifically, the rapid localization of the photo-hole (h_{VB}) from the valence band into the Au^+ centre optically converts it into a doubly charged Au^{2+} cation following the reaction $\text{Au}^+(d^{10}) + h_{\text{VB}} \rightarrow \text{Au}^{2+}(d^9)$. The resulting *sp-d* exchange interaction between the unpaired spin in the incomplete *d*-shell of Au^{2+} and the host material's conduction/valence bands effectively turns the NCs into optically-activated DMS nanomaterials.

In order to investigate this photo-induced magnetic behaviour we performed MCD spectroscopy, which measures the Zeeman splitting of the 1S exciton absorption peak. In particular, MCD can reveal the presence of paramagnetic dopants in the semiconductor host, via the appearance of an enhanced and temperature-dependent Zeeman splitting that arises from *sp-d* spin exchange coupling between the paramagnetic dopants and the 1S exciton⁸¹. In our specific case, the probe light used in the MCD experiments, being resonant with the NC's absorption spectrum, also generates the paramagnetic species by photoexciting the NCs. **Figure 5a** presents the MCD spectra of the Au:CdSe NCs as a function of the applied magnetic field, *B*, and temperature. The derivative-like spectrum is featured by two peaks at ~ 2.4 eV and ~ 2.75 eV corresponding to the Zeeman splitting of the 1S and 2S exciton

spin states, respectively. The magnetic response intensifies strongly with increasing B from zero to 7 T (at 2.85 K) and also upon lowering the temperature from 40 to 2.85 K (at B=6 T).

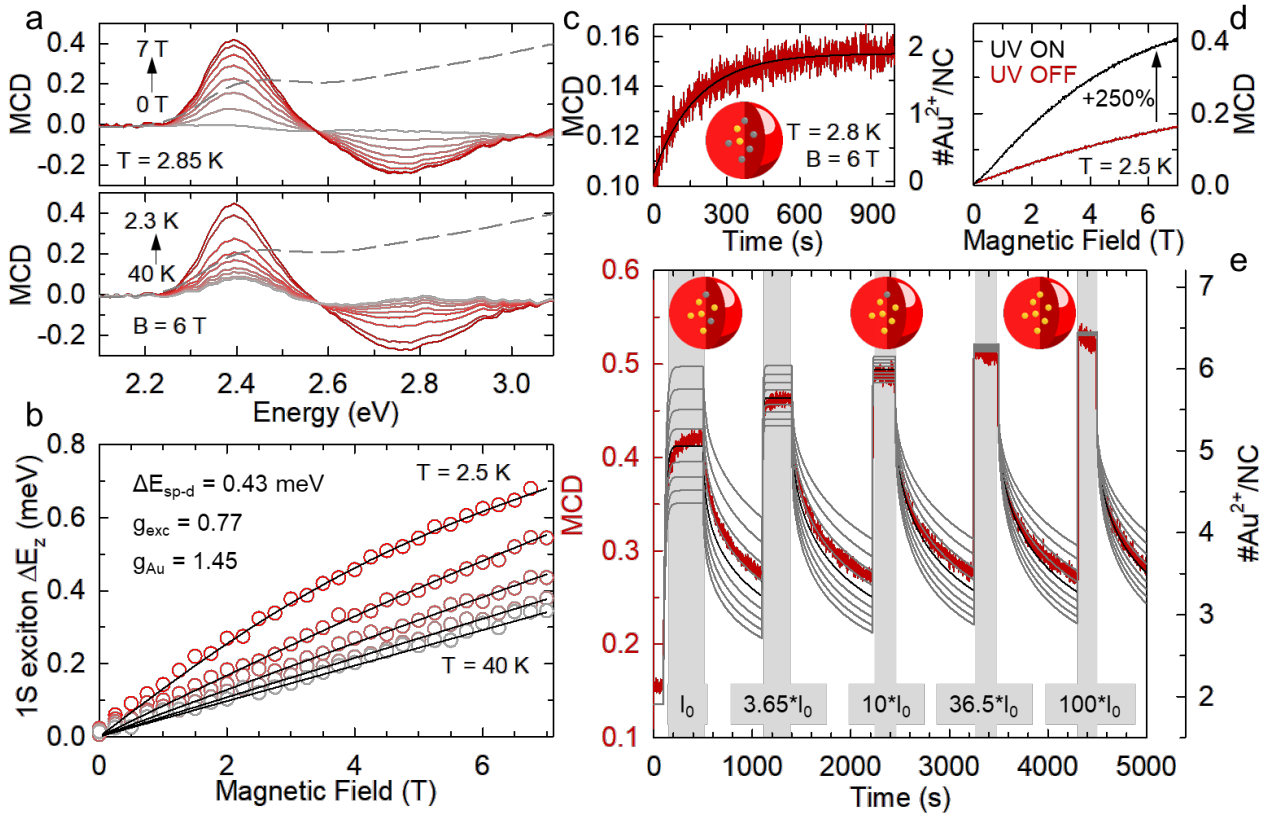


Figure 5. Magnetic properties of Au:CdSe NCs. The scheme of the experimental setup is sketched in Supporting Figure S16. (a) MCD spectra of Au:CdSe NCs, from which the Zeeman splitting of the 1S exciton can be inferred. Top panel: MCD spectra are shown at 2.85 K in different magnetic fields from 0 to 7 T. Bottom panel: MCD spectra at 6 T, at temperatures from 40 to 2.3 K. The linear absorption spectrum is reported as a dashed grey line in a and b. (b) Enhanced Zeeman splitting of the 1S band-edge exciton versus magnetic field, at various temperatures. The high field saturation and strong temperature dependence indicate the existence of *sp-d* exchange coupling between the conduction/valence bands of the semiconductor host and paramagnetic dopants in the NCs. This species is consistent with Au²⁺ dopants excited by fast localization (capture) of the VB hole. Lines are fits to a Brillouin function using a single set of parameters. (c) Evolution of the MCD signal of the 1S exciton of Au:CdSe NCs over time, measured at 2.8 K and 6 T using 25 nW/cm² probe fluence. The black line represents the average number of photoexcited Au²⁺ species following the dynamic model described in the main text reaching saturation at ~2 Au²⁺ per NC. (d) Peak MCD signal (measured at 2.4 eV) as a continuous function of applied magnetic field with and without additional UV illumination (40 μWcm⁻²). (e) Time evolution of the MCD signal as additional UV illumination is turned on (grey shading, I₀ = 0.3 μW) and off. Stronger UV intensity leads to larger MCD signal and faster dynamics of both on and off phases. In all cases, the MCD decay is markedly slower than the corresponding rise under UV excitation. The grey curves are the average number of paramagnetic centres calculated through the kinetic model explained in the main text using different *k*-values ranging from 0.0266 to 0.0506 s⁻¹ with 0.003 s⁻¹ steps. The black line is the solution of the kinetic model using the experimental *k*-value of 0.0386 s⁻¹. The MCD approaches saturation when the number of paramagnetic species per NC in kinetic equilibrium approaches seven, in agreement with the quantized doping level of the NC.

The temperature-dependent MCD unambiguously indicates *sp-d* coupling between the 1S exciton and paramagnetic impurities in the NCs, because the average magnetization of a paramagnet depends strongly on both field and temperature. The effect is quantified in **Figure 5b**, where we report the splitting of the 1S exciton (E_{probe}=2.39 eV) as a function of B at several temperatures, clearly showing strong temperature-dependence and saturation of the splitting energy. Both these behaviours are

definitive signatures of *sp-d* exchange. Accordingly, the experimental data are well fitted with the standard Brillouin function for conventional DMS materials⁸²:

$$\Delta E_Z = g_{ex}\mu_B B + \Delta E_{sp-d}\langle S_Z \rangle, \quad \text{Eq.1}$$

where the first term represents the intrinsic, temperature-independent linear Zeeman splitting of the CdSe exciton states determined solely by the exciton *g*-factor (g_{ex}), and the second term considers any additional splitting due to the *sp-d* exchange interaction with the Au²⁺ impurities, which are characterized by a temperature-dependent average spin projection along *B* ($\langle S_Z \rangle$). We describe the field- and temperature-dependent paramagnetism of spin-*J* ions $\langle S_Z \rangle$ with the Brillouin function $B_J(g_{Au}\mu_B J B / k_B T)$, where g_{Au} is the Landé factor of the unpaired spin at the Au²⁺ ion, μ_B is the Bohr magneton and k_B the Boltzmann constant. In II-VI semiconductors, the tetrahedral crystal field splits the *d*-states of the impurities in a sixfold degenerate t_{2g} state (at lower energies) and a fourfold degenerate e_g state (at higher energies). The Au-spin is therefore featured by $J=1/2$, which has been used to fit the experimental data in **Figure 5b** with Eq.(1). g_{ex} , g_{Au} and ΔE_{sp-d} have also been set as shared parameters and the best fit has been obtained using $\Delta E_{sp-d}=0.43$ meV, $g_{Au}=1.45$ and $g_{ex}=0.77$. The CdSe exciton *g*-factor is in agreement with previous results obtained via magneto-optical investigation of undoped CdSe NCs.⁸³ As per the Landé factor of Au²⁺, the obtained value is consistent with previous results for Cu²⁺ and Ag²⁺ impurities with similar open d^9 configuration^{19, 20}. Importantly, in agreement with the mechanistic picture of **Figure 2a**, the observed magnetic response is not an intrinsic ground state feature of Au:CdSe NCs, but is rather a direct consequence of their illumination by light - in this case the weak probe light that is used to measure MCD. This is clearly demonstrated in **Figure 5c** showing progressive intensification of the 1S MCD signal as a function of the illumination time by the probe beam at 2.4 eV (25 nW/cm²), reaching saturation after ~10 minutes. The black line is the theoretical simulation of the number of Au²⁺ paramagnetic species per NC obtained through the kinetic model described below. In these weak illumination conditions, equilibrium is achieved when each NC contains on average 1.9 Au²⁺ species. In order to further emphasize this effect, in **Figure 5d** we show the evolution of the 1S MCD intensity as a function of *B* in the absence and in the presence of additional excitation with UV light (3.1 eV, 40 μW/cm²) leading to over 250% enhancement of the MCD with respect to the case of probe light only. In order to investigate the dynamics of the photo-magnetization mechanism and to correlate it to the quantized doping level of the NCs, we monitored the evolution of the MCD signal in successive ON/OFF UV illumination scans. In this experiment (the experimental setup is sketched in Supporting **Figure S16**), the weak probe light is kept constant for the whole duration of the measurement (25 nW/cm² as in **Figure 5c**), whereas the additional UV fluence is increased at each cycle from 0.4, 1.5, 4, 15 to 40 μW/cm². Before performing the first UV cycle, the sample was illuminated by the probe light in order

to reach saturation of the photo-magnetization following the trend in **Figure 5c**. As shown in **Figure 5e**, increasing the fluence of the UV light results in higher MCD saturation values and faster magnetization/demagnetization kinetics. For all fluences used, when the UV light is turned off, the MCD signal decreases slowly over several minutes, indicating that the persistence of the metastable paramagnetic state is not limited by the lifetime of the Au-PL but is likely determined by the release time of trapped electrons in surface defects, similar to what is observed for Cu⁺ or Ag⁺ doped NCs^{19, 20}.

This assignment is in agreement with the spectro-electrochemistry measurements in **Figure 2c** showing over 50% brightening of the Au-PL upon raising the NC Fermi energy, which is indicative of the presence of localized states below the NC conduction band acting as efficient electron traps. A closer look at the MCD kinetics in Figure 3e reveals the presence of two main decay trends, possibly associated to detrapping of electrons from intragap traps with different depth. Finally, we use the MCD data in **Figure 5c** and **5e** to model the evolution in time of the average number of paramagnetic centres associated to Au²⁺ cations when the sample is illuminated with the probe beam and by the additional UV light through the expression:

$$\frac{dP(t)}{dt} = \langle N \rangle * \phi_{HC} - k(\langle N \rangle) * P(t) \quad (2)$$

where $\langle N \rangle = \langle N \rangle_{Probe} + \langle N \rangle_{UV} = \sigma_{1S} * f_{Probe} + \sigma_{3.1eV} * f_{UV}$ is the average number of excitons generated per unit time by continuous illumination (considering the exciton emission lifetime of 290 ns, **Table S3**) in a NC with absorption cross section σ (respectively at the 1S energy, $\sigma_{1S}=3.9 \times 10^{-16}$ cm² and at 3.1 eV, $\sigma_{3.1eV}=1.0 \times 10^{-15}$ cm²)⁶³ by a probe fluence (f_{Probe}) and by an additional UV fluence (f_{UV}). ϕ_{HC} is the capture efficiency of a VB hole in an Au⁺ centre, k is the relaxation rate of the Au²⁺ centres to the nonmagnetic Au⁺ state (experimentally found to depend on the excitation conditions) and $P(t)$ is the number of photo-generated Au²⁺ species. The first term on the right side of Eq.(2) represents the number of the Au²⁺ paramagnetic centres generated per unit time and the second term is the relaxation of the photo-activated Au²⁺ ions back to their Au⁺ ground state. By using the experimental value of $\langle N \rangle$, a decay rate $k=3.86 \times 10^{-2}$ s⁻¹ and assuming that $\phi_{HC} \sim 100\%$, the trend of the MCD response in **Figure 5e** is simply reproduced yielding a saturation $P(t)$ -value of 1.9 Au²⁺/NC due solely by the probe beam. The same model also describes the behaviour under UV illumination, with the term $\langle N \rangle$ now resulting from both the probe light and the additional UV excitation that accounts for most of the generated Au²⁺ over time. In order to best describe the decay trend of the MCD signal when the UV laser is switched off, the decay rate k that appears to be growing with the UV fluence, has been extracted from the fast portion of the experimental MCD decay for each f_{UV} used. To further emphasize the role of k in the paramagnetic response of the Au:CdSe NCs, we

calculated the rise and decay trends by varying the k -values by $\pm 0.012 \text{ s}^{-1}$ (0.003 s^{-1} steps), resulting in the grey curves in **Figure 5e**. We notice that, given the very slow demagnetization kinetics that prevented us from performing MCD measurements until full decay of the magnetic response, the initial number of Au^{2+} species per NC in successive ON/OFF cycles has been set as the calculated value after the decay of the previous cycle. Remarkably, with no other free parameter except the decay rate in the presence of the probe light only, this simple model describes the MCD response and shows that the system approaches equilibrium saturation when nearly all seven Au^+ dopants are photo-converted to Au^{2+} . We finally notice that increasing the UV fluence further was not possible as that would lead to artefacts due to sample heating effects.

In conclusion, we have produced the first example of colloidal NCs electronically doped with gold impurities using a fully redesigned quantized doping approach that enables us to directly synthesize homogeneous NC ensembles where each particle contains an exact predetermined number of electronic impurities. The NCs are thoroughly characterized for their structural, optical and magnetic properties, showing distinct signatures of dopant related physical processes directly related to their quantized doping level. The approach that we have demonstrated with Au clusters is not size- or host-specific and could, in principle, be applied to different monometallic or alloyed clusters, allowing the realization of charge engineered NCs with predesigned optical, magnetic and electronic properties for future fundamental studies and advanced optoelectronic, photonic and spintronic devices.

References

- (1) Kovalenko, M. V.; Manna, L.; Cabot, A.; Hens, Z.; Talapin, D. V.; Kagan, C. R.; Klimov, V. I.; Rogach, A. L.; Reiss, P.; Milliron, D. J.; Guyot-Sionnest, P.; Konstantatos, G.; Parak, W. J.; Hyeon, T.; Korgel, B. A.; Murray, C. B.; Heiss, W. *ACS Nano* **2015**, *9*, (2), 1012-1057.
- (2) Gao, Y.; Tang, Z. *Small* **2011**, *7*, (15), 2133-2146.
- (3) Boles, M. A.; Engel, M.; Talapin, D. V. *Chem. Rev.* **2016**, *116*, (18), 11220-11289.
- (4) Grzelczak, M.; Vermant, J.; Furst, E. M.; Liz-Marzán, L. M. *ACS Nano* **2010**, *4*, (7), 3591-3605.
- (5) Owen, J.; Brus, L. *J. Am. Chem. Soc.* **2017**, *139*, (32), 10939-10943.
- (6) De Trizio, L.; Manna, L. *Chem. Rev.* **2016**, *116*, (18), 10852-10887.
- (7) Reiss, P.; Carrière, M.; Lincheneau, C.; Vaure, L.; Tamang, S. *Chem. Rev.* **2016**, *116*, (18), 10731-10819.
- (8) Boles, M. A.; Ling, D.; Hyeon, T.; Talapin, D. V. *Nat. Mater.* **2016**, *15*, 141.
- (9) Pietryga, J. M.; Park, Y.-S.; Lim, J.; Fidler, A. F.; Bae, W. K.; Brovelli, S.; Klimov, V. I. *Chem. Rev.* **2016**, *116*, (18), 10513-10622.
- (10) Talapin, D. V.; Lee, J. S.; Kovalenko, M. V.; Shevchenko, E. V. *Chem. Rev.* **2010**, *110*, (1), 389-458.
- (11) Carey, G. H.; Abdelhady, A. L.; Ning, Z.; Thon, S. M.; Bakr, O. M.; Sargent, E. H. *Chem. Rev.* **2015**, *115*, (23), 12732-63.
- (12) Brovelli, S.; Galland, C.; Viswanatha, R.; Klimov, V. I. *Nano Lett.* **2012**, *12*, (8), 4372-4379.
- (13) Bradshaw, L. R.; Knowles, K. E.; McDowall, S.; Gamelin, D. R. *Nano Lett.* **2015**, *15*, (2), 1315-1323.
- (14) Sharma, M.; Gungor, K.; Yeltik, A.; Olutas, M.; Guzelurk, B.; Kelestemur, Y.; Erdem, T.; Delikanli, S.; McBride James, R.; Demir Hilmi, V. *Adv. Mater.* **2017**, *29*, (30), 1700821.
- (15) Kang, M. S.; Sahu, A.; Frisbie, C. D.; Norris, D. J. *Adv. Mater.* **2013**, *25*, (5), 725-731.
- (16) Sahu, A.; Braga, D.; Waser, O.; Kang, M. S.; Deng, D.; Norris, D. J. *Nano Lett.* **2013**, *14*, (1), 115-121.

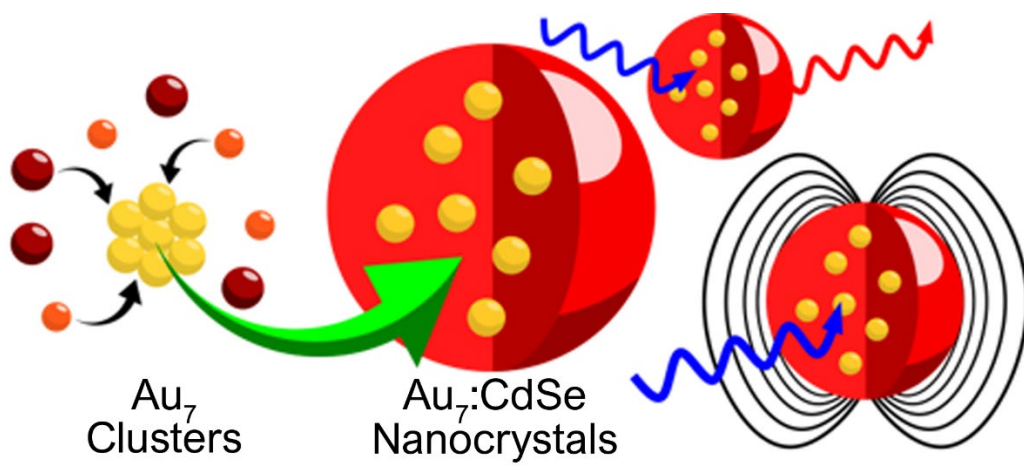
- (17) Choi, J.-H.; Wang, H.; Oh, S. J.; Paik, T.; Sung, P.; Sung, J.; Ye, X.; Zhao, T.; Diroll, B. T.; Murray, C. B.; Kagan, C. R. *Science* **2016**, 352, (6282), 205-208.
- (18) Choi, J.-H.; Oh, S. J.; Lai, Y.; Kim, D. K.; Zhao, T.; Fafarman, A. T.; Diroll, B. T.; Murray, C. B.; Kagan, C. R. *ACS Nano* **2013**, 7, (9), 8275-8283.
- (19) Pandey, A.; Brovelli, S.; Viswanatha, R.; Li, L.; Pietryga, J. M.; Klimov, V. I.; Crooker, S. A. *Nat. Nanotech.* **2012**, 7, 792-797.
- (20) Pinchetti, V.; Di, Q.; Lorenzon, M.; Camellini, A.; Fasoli, M.; Zavelani-Rossi, M.; Meinardi, F.; Zhang, J.; Crooker, S. A.; Brovelli, S. *Nat. Nanotech.* **2018**, 13, (2), 145-151.
- (21) Viswanatha, R.; Brovelli, S.; Pandey, A.; Crooker, S. A.; Klimov, V. I. *Nano Lett.* **2011**, 11, (11), 4753-4758.
- (22) Geiregat, P.; Houtepen, A. J.; Sagar, L. K.; Infante, I.; Zapata, F.; Grigel, V.; Allan, G.; Delerue, C.; Van Thourhout, D.; Hens, Z. *Nat. Mater.* **2017**, 17, 35.
- (23) Wu, K.; Park, Y.-S.; Lim, J.; Klimov, V. I. *Nat. Nanotech.* **2017**, 12, 1140.
- (24) Sahu, A.; Kang, M. S.; Kompch, A.; Notthoff, C.; Wills, A. W.; Deng, D.; Winterer, M.; Frisbie, C. D.; Norris, D. J. *Nano Lett.* **2012**, 12, (5), 2587-2594.
- (25) Voznyy, O.; Zhitomirsky, D.; Stadler, P.; Ning, Z.; Hoogland, S.; Sargent, E. H. *ACS Nano* **2012**, 6, (9), 8448-8455.
- (26) Stavrinadis, A.; Rath, A. K.; de Arquer, F. P. G.; Diedenhofen, S. L.; Magén, C.; Martínez, L.; So, D.; Konstantatos, G. *Nat. Commun.* **2013**, 4, 2981.
- (27) Kirmani, A. R.; Kiani, A.; Said, M. M.; Voznyy, O.; Wehbe, N.; Walters, G.; Barlow, S.; Sargent, E. H.; Marder, S. R.; Amassian, A. *ACS Energy Lett.* **2016**, 1, (5), 922-930.
- (28) Luther, J. M.; Jain, P. K.; Ewers, T.; Alivisatos, A. P. *Nat. Mater.* **2011**, 10, 361.
- (29) Liu, J.; Zhao, Q.; Liu, J.-L.; Wu, Y.-S.; Cheng, Y.; Ji, M.-W.; Qian, H.-M.; Hao, W.-C.; Zhang, L.-J.; Wei, X.-J.; Wang, S.-G.; Zhang, J.-T.; Du, Y.; Dou, S.-X.; Zhu, H.-S. *Adv. Mater.* **2015**, 27, (17), 2753-2761.
- (30) Kroupa, D. M.; Hughes, B. K.; Miller, E. M.; Moore, D. T.; Anderson, N. C.; Chernomordik, B. D.; Nozik, A. J.; Beard, M. C. *J. Am. Chem. Soc.* **2017**, 139, (30), 10382-10394.
- (31) Kompch, A.; Sahu, A.; Notthoff, C.; Ott, F.; Norris, D. J.; Winterer, M. *J. Phys. Chem. B* **2015**, 119, (32), 18762-18772.
- (32) Mocatta, D.; Cohen, G.; Schattner, J.; Millo, O.; Rabani, E.; Banin, U. *Science* **2011**, 332, (6025), 77-81.
- (33) Srivastava, B. B.; Jana, S.; Pradhan, N. *J. Am. Chem. Soc.* **2011**, 133, (4), 1007-1015.
- (34) Xie, R.; Peng, X. *J. Am. Chem. Soc.* **2009**, 131, (30), 10645-10651.
- (35) Tuinenga, C.; Jasinski, J.; Iwamoto, T.; Chikan, V. *ACS Nano* **2008**, 2, (7), 1411-1421.
- (36) Roy, S.; Tuinenga, C.; Fungura, F.; Dagtepe, P.; Chikan, V.; Jasinski, J. *J. Phys. Chem. B* **2009**, 113, (30), 13008-13015.
- (37) Bindra, J. K.; Kurian, G.; Christian, J. H.; Van Tol, J.; Singh, K.; Dalal, N. S.; Mochena, M. D.; Stoian, S. A.; Strouse, G. F. *Chem. Mater.* **2018**, 30, (23), 8446-8456.
- (38) Wills, A. W.; Kang, M. S.; Wentz, K. M.; Hayes, S. E.; Sahu, A.; Gladfelter, W. L.; Norris, D. J. *J. Mater. Chem.* **2012**, 22, (13), 6335.
- (39) Avdonin, A. N.; Ivanova, G. N.; Nedeoglo, D. D.; Nedeoglo, N. D.; Sirkeli, V. P. *Physica B* **2005**, 365, (1), 217-224.
- (40) Chacham, H.; Alves, J. L. A.; De Siqueira, M. L. *Solid State Commun.* **1986**, 60, (5), 411-414.
- (41) Dean, P. J.; Fitzpatrick, B. J.; Bhargava, R. N. *Phys. Rev. B* **1982**, 26, (4), 2016-2035.
- (42) Poolton, N. R. J.; Davies, J. J.; Nicholls, J. E.; Fitzpatrick, B. J. *J. Phys. C* **1987**, 20, (23), 3553.
- (43) Poolton, N. R. J.; Nicholls, J. E.; Davies, J. J. *J. Cryst. Growth* **1988**, 86, (1), 609-614.
- (44) Magnea, N.; Bensahel, D.; Pautrat, J. L.; Pfister, J. C. *Phys. Status Solidi B* **1979**, 94, (2), 627-639.
- (45) Mokari, T.; Aharoni, A.; Popov, I.; Banin, U. *Angew. Chem.* **2006**, 45, (47), 8001-8005.
- (46) Buonsanti, R.; Milliron, D. J. *Chem. Mater.* **2013**, 25, (8), 1305-1317.
- (47) Norris, D. J.; Efros, A. L.; Erwin, S. C. *Science* **2008**, 319, (5871), 1776-1779.
- (48) Erwin, S. C.; Zu, L. J.; Haftel, M. I.; Efros, A. L.; Kennedy, T. A.; Norris, D. J. *Nature* **2005**, 436, (7047), 91-94.
- (49) Chen, D.; Viswanatha, R.; Ong, G. L.; Xie, R.; Balasubramanian, M.; Peng, X. *J. Am. Chem. Soc.* **2009**, 131, (26), 9333-9339.
- (50) Jawaid, A. M.; Chattopadhyay, S.; Wink, D. J.; Page, L. E.; Snee, P. T. *ACS Nano* **2013**, 7, (4), 3190-3197.
- (51) Santiago-González, B.; Monguzzi, A.; Pinchetti, V.; Casu, A.; Prato, M.; Lorenzi, R.; Campione, M.; Chiodini, N.; Santambrogio, C.; Meinardi, F.; Manna, L.; Brovelli, S. *ACS Nano* **2017**, 11, (6), 6233-6242.

- (52) Hassan, A.; Zhang, X.; Liu, X.; Rowland, C. E.; Jawaid, A. M.; Chattopadhyay, S.; Gulec, A.; Shamirian, A.; Zuo, X.; Klie, R. F.; Schaller, R. D.; Snee, P. T. *ACS Nano* **2017**, 11, (10), 10070-10076.
- (53) Ye, X.; Reifsnnyder Hickey, D.; Fei, J.; Diroll, B. T.; Paik, T.; Chen, J.; Murray, C. B. *J. Am. Chem. Soc.* **2014**, 136, (13), 5106-15.
- (54) Hassan, A.; Zhang, X.; Liu, C.; Snee, P. T. *J. Phys. Chem. B* **2018**, 122, (20), 11145-11151.
- (55) Luo, Z.; Yuan, X.; Yu, Y.; Zhang, Q.; Leong, D. T.; Lee, J. Y.; Xie, J. *J. Am. Chem. Soc.* **2012**, 134, (40), 16662-70.
- (56) de Heer, W. A. *Rev. Mod. Phys.* **1993**, 65, (3), 611-676.
- (57) Stamplecoskie, K. G.; Kamat, P. V. *J. Am. Chem. Soc.* **2014**, 136, (31), 11093-11099.
- (58) Darrah Thomas, T.; Weightman, P. *Phys. Rev. B* **1986**, 33, (8), 5406-5413.
- (59) Casaletto, M. P.; Longo, A.; Martorana, A.; Prestianni, A.; Venezia, A. M. *Surf. Interface Anal.* **2006**, 38, (4), 215-218.
- (60) Yang, Y. A.; Wu, H.; Williams, K. R.; Cao, Y. C. *Angew. Chem. Int. Ed.* **2005**, 44, (41), 6712-6715.
- (61) Häkkinen, H. *Chem. Soc. Rev.* **2008**, 37, (9), 1847-1859.
- (62) Gruene, P.; Rayner, D. M.; Redlich, B.; van der Meer, A. F. G.; Lyon, J. T.; Meijer, G.; Fielicke, A. *Science* **2008**, 321, (5889), 674-676.
- (63) Yu, W. W.; Qu, L.; Guo, W.; Peng, X. *Chem. Mater.* **2003**, 15, (14), 2854-2860.
- (64) Knowles, K. E.; Hartstein, K. H.; Kilburn, T. B.; Marchioro, A.; Nelson, H. D.; Whitham, P. J.; Gamelin, D. R. *Chem. Rev.* **2016**, 116, (18), 10820-10851.
- (65) Aven, M.; Segall, B. *Phys. Rev.* **1963**, 130, (1), 81-91.
- (66) Georgobiani, A. N.; Aminov, U. A.; Dravin, V. A.; Lepnev, L. S.; Mullabaev, I. D.; Ursaki, V. V.; Iljukhina, Z. P. *Nucl. Instrum. Methods Phys. Res., Sect. A* **1999**, 426, (1), 164-168.
- (67) Nedeoglo, N. D.; Avdonin, A. N.; Ivanova, G. N.; Nedeoglo, D. D.; Kolibaba, G. V.; Sirkeli, V. P. *J. Lumin.* **2005**, 112, (1), 62-65.
- (68) Avinor, M.; Meijer, G. *J. Chem. Phys.* **1960**, 32, (5), 1456-1458.
- (69) Poolton, N. R. J. *J. Phys. C* **1987**, 20, (34), 5867.
- (70) Lorenzon, M.; Sortino, L.; Akkerman, Q.; Accornero, S.; Pedrini, J.; Prato, M.; Pinchetti, V.; Meinardi, F.; Manna, L.; Brovelli, S. *Nano Lett.* **2017**.
- (71) Galland, C.; Ghosh, Y.; Steinbrueck, A.; Sykora, M.; Hollingsworth, J. A.; Klimov, V. I.; Htoon, H. *Nature* **2011**, 479, 203-207.
- (72) Jha, P. P.; Guyot-Sionnest, P. *ACS Nano* **2009**, 3, (4), 1011-1015.
- (73) Makarov, N. S.; McDaniel, H.; Fuke, N.; Robel, I.; Klimov, V. I. *J. Phys. Chem. Lett.* **2014**, 5, (1), 111-8.
- (74) Padilha, L. A.; Bae, W. K.; Klimov, V. I.; Pietryga, J. M.; Schaller, R. D. *Nano Lett.* **2013**, 13, (3), 925-932.
- (75) Yu, W. W.; Peng, X. *Angew. Chem.* **2002**, 41, (13), 2368-2371.
- (76) Siy, J. T.; Bartl, M. H. *Chem. Mater.* **2010**, 22, (21), 5973-5982.
- (77) Jasieniak, J.; Smith, L.; van Embden, J.; Mulvaney, P.; Califano, M. *J. Phys. Chem. B* **2009**, 113, (45), 19468-19474.
- (78) Klimov, V. I.; Mikhailovsky, A. A.; McBranch, D. W.; Leatherdale, C. A.; Bawendi, M. G. *Science* **2000**, 287, (5455), 1011-1013.
- (79) Yang, C.; Faust, A.; Amit, Y.; Gdor, I.; Banin, U.; Ruhman, S. *J. Phys. Chem. A* **2016**, 120, 3088-3097.
- (80) Kuno, M.; Nirmal, M.; Bawendi, M. G.; Efros, A.; Rosen, M. *J. Chem. Phys.* **1998**, 108, (10), 4242-4247.
- (81) Bussian, D. A.; Crooker, S. A.; Yin, M.; Brynda, M.; Efros, A. L.; Klimov, V. I. *Nat. Mater.* **2009**, 8, (1), 35-40.
- (82) Furdyna, J. K. *J. Appl. Phys.* **1988**, 64, (4), R29-R64.
- (83) Johnston-Halperin, E.; Awschalom, D. D.; Crooker, S. A.; Efros, A. L.; Rosen, M.; Peng, X.; Alivisatos, A. P. *Phys. Rev. B* **2001**, 63, (20), 205309.

Acknowledgments

The authors thank Professor Liberato Manna of the Italian Institute of Technology for valuable assistance in the structural and chemical analysis of the NC. Work at the NHMFL was supported by NSF DMR-1644779, the State of Florida, and the US DOE. A.C. and M.Z.-R. acknowledge the project MIUR-PRIN 2015 Grant No. 2015WTW7J3 for financial support

TOC Figure



Quantized electronic doping towards atomically controlled 'charge-engineered' semiconductor nanocrystals

Chiara Capitani,^{1,2†} Valerio Pinchetti,^{1†} Graziella Gariano,² Beatriz Santiago-González,^{1,3} Carlo Santambrogio,⁴ Marcello Campione,⁵ Mirko Prato,⁶ Rosaria Brescia,⁶ Andrea Camellini,⁷ Fulvio Bellato,¹ Francesco Carulli,¹ Abhinav Anand,¹ Margherita Zavelani-Rossi,⁷ Francesco Meinardi,^{1,2} Scott A. Crooker,^{8} Sergio Brovelli.^{1,2*}*

¹ Dipartimento di Scienza dei Materiali, Università degli Studi di Milano – Bicocca, Via R. Cozzi 55, I-20125, Milano, Italy;

² Glass to Power SpA, Via F. Daverio 6, I-20135, Milano, Italy;

³ International Iberian Nanotechnology Laboratory, Nanophotonics Department, Ultrafast Bio- and Nanophotonics Group, Avenida Mestre José Veiga s/n 4715-330 Braga, Portugal;

⁴ Dipartimento di Biotecnologie e Bioscienze, Università degli Studi di Milano – Bicocca, Piazza della Scienza 2, I-20126 Milano, Italy;

⁵ Dipartimento di Scienze dell'Ambiente e del Territorio e di Scienze della Terra, Università degli Studi Milano-Bicocca, Piazza della Scienza, I-20125 Milano, Italy;

⁶ Istituto Italiano di Tecnologia, Via Morego 30, 16163 Genova, Italy;

⁷ Dipartimento di Energia, Politecnico di Milano and IFN-CNR, Milano, Italy.

⁸ National High Magnetic Field Laboratory, Los Alamos National Laboratory, Los Alamos, New Mexico, 87545, United States.

[†] These authors contributed equally to this work.

Methods

Chemicals

Gold(III) chloride hydrate, (99.99%), L-glutathione, GSH, ($\geq 98\%$), tetrabutylammonium bromide, TOABr, ($\geq 98\%$), 1-dodecanethiol, DDT, ($\geq 98\%$), ultrapure water (Chromasolv Plus, for HPLC), sodium myristate ($\geq 99\%$), selenium powder-100 mesh (99.99%), oleic acid, OA ($\geq 90\%$), cadmium nitrate tetrahydrate ($\geq 98\%$), gold(I) chloride ($\geq 99\%$), 2-propanol ($\geq 99.8\%$), ethanol ($\geq 99.8\%$), methanol ($\geq 99.8\%$), toluene ($\geq 99.5\%$), 1-octadecene, ODE ($\geq 90\%$), were purchased from Sigma-Aldrich and gold(III) acetate ($\geq 99.99\%$) from Alfa Aesar.

Synthesis of Au₇ Clusters - The synthesis of Au₇-GSH clusters was carried out following a published procedure.¹ In 17.4 mL of ultrapure water were added 2 mL of HAuCl₄ (0.02 M) and 0.6 mL of L-glutathione (GSH, 0.1 M). After 24 hours of vigorous stirring at 70°C, the clusters were purified by adding isopropanol to the solution (1:2 volume ratio) and centrifuged at 6500 rpm for 20 minutes. This procedure was repeated thrice and the purified clusters are then dispersed in ultrapure water.

Ligand exchange – In the 5 mL of Au₇-GSH solution (76 μ M) were added ~ 0.3 mL of NaOH 1 M until the solution had pH ~ 9.0 and 5 mL of TOABr, 0.02 M in ethanol. After 2 minutes of vigorous stirring, 5 mL of DDT (0.15 M) in toluene were also added. The mixture was then heated to 70°C and kept under vigorous stirring for 1 hour. The organic phase was separated and washed thrice with ultrapure water to remove water-soluble impurities. After the Au₇-DDT were dispersed in ODE.

Synthesis of CdSe and Au:CdSe - The synthesis of CdSe NCs was carried out following a published procedure². The Cd-myristate precursor was prepared via ex-situ method: a solution of cadmium nitrate in methanol (0.05 M, 40 mL) was added to a solution of sodium myristate in methanol (0.025 M, 240 mL). The white precipitate was washed twice with methanol and dried under vacuum to remove all solvents. 0.1 mmol Cd-myristate were then added to 0.05 mmol Se powder in a 25 mL flask with 6.38 mL of ODE and 1 mL of OA and exposed to vacuum for 15 minutes. Successively heated to 210°C for 1 hour under N₂ flow. The samples were finally purified twice with hexane/ethanol co-solvents by centrifugation (4500 rpm, 10 min) to remove excess ligands and unreacted precursor. The synthesis route for the doped NCs is the same, adding 2.5 mL of Au₇-DDT 76 μ M to the reaction mixture.

Etching experiments – The experiments were conducted following the procedure from ref.^{3, 4}. Specifically, 0.5 mL of OA were added to 0.5 mL of Au:CdSe NCs toluene solution 10 mg/mL. The mixture was then heated to 90-100°C for 140 minutes.

Structural Characterization

Electrospray Ionization Mass Spectrometry - ESI-MS experiments in positive-ion mode were performed on a hybrid quadrupole/time-of-flight instrument equipped with a nanoelectrospray ion source (AB Sciex, Foster City, CA, USA). The samples were infused by borosilicate-coated capillaries of 1 μ m internal diameter (Thermo Fisher Scientific, Waltham, MA, USA). The main instrumental parameters were as follows: ion-spray voltage 1.1 kV; curtain gas 20 psi; declustering potential 80 V. The recorded spectra were averaged over a 1 min acquisition time. The simulation of the peak distributions of the ESI-MS spectra was performed by IsoPro 3.1 based on the Yergey algorithm⁵.

X-ray Photoelectron Spectroscopy - XPS Measurements were performed on a Kratos Axis Ultra^{DLD} spectrometer using a monochromatic Al K α source operated at 15 kV and 20 mA. The specimen for XPS was prepared by drop casting 200 μ L of a clean and concentrated sample solution onto a silicon wafer, thus obtaining a circular drop (approximately 1 cm wide in diameter) on it. All the analyses were carried out over an area of 300 \times 700 μ m. High-resolution analyses were carried out with a pass energy of 10 eV. The Kratos charge neutralizer system was used during data acquisition. Spectra have been charge corrected to the main line of the carbon 1s spectrum set to 284.8 eV (C–C bond). Spectra were analyzed using Casa XPS software (version 2.3.16).

High-Resolution Transmission Electron Microscopy - HR-TEM imaging was performed on a JEOL JEM-2200FS microscope equipped with a field emission gun working at an accelerating voltage of 200 kV, a CEOS spherical aberration corrector of the objective lens, allowing to reach a spatial resolution of 0.9 Å, and an in-column Omega filter.

Powder X-ray Diffraction - Powder XRD patterns were acquired in Bragg–Brentano geometry with Cu K α radiation (Panalytical X'Pert Pro powder diffractometer).

Inductively Coupled Plasma Atomic Emission Spectroscopy - ICP-AES was carried out using a iCAP 6500 Thermo spectrometer. All chemical analyses performed by ICP-AES were affected by a systematic error of about 5%. Samples were dissolved in HCl/HNO₃ 3:1 (v/v).

Optical Characterization

Optical absorption - Optical absorption spectra were recorded at room temperature on a Varian Cary 50 Scan UV–visible spectrophotometer under normal incidence in cuvettes (optical path 0.1 cm).

Photoluminescence measurements - PL measurements were performed using a pulsed diode laser at 3.1 eV (Edinburgh Inst. EPL 405, 40 ps pulse width) as excitation source and collecting the emitted light with a TM-C10083CA Hamamatsu Mini-Spectrometer. Time-resolved PL experiments were conducted using the same excitation source and collecting with a Hamamatsu R943-02 time-correlated single-photon counting unit coupled to an Oriel Instruments Cornerstone 260 monochromator. All PL measurements were performed with a power density of 100 nJ cm⁻². Power-dependent PL spectra were acquired using a Minilite Continuum Laser as excitation source (3.5 eV, 15 Hz, 5 ns pulse width) and collecting the emitted light with a TM-C10083CA Hamamatsu Mini-Spectrometer.

Transient transmission spectroscopy - For the ultrafast transient transmission measurements, the laser source was a Ti:sapphire laser with chirped pulse amplification (Coherent LIBRA-HE), which provided 95 fs pulses at 800 nm at a repetition rate of 2 kHz. The excitation pulses at 400 nm were generated by second harmonic generation of the fundamental beam. The bandwidth of the pump pulses is 10nm which correspond to a pulse duration ~100fs. The probe beam was a white light supercontinuum generated by focusing a small fraction of the fundamental beam onto a 2mm thick sapphire plate. The supercontinuum spectrum extends from 450 nm to 1.6 μ m, with a gap only around the fundamental wavelength at 800 nm. Pump and probe are then focused on the sample by means of a lens and a spherical mirror.

A computer-controlled optical multichannel analyser working at 1kHz acquires the map of the differential transmission $\Delta T/T = (T_{on} - T_{off})/T_{off}$, as a function of the pump–probe time delay; T_{on} and T_{off} are the probe spectra transmitted by the excited and unperturbed samples.

Spectro-electrochemical measurements - ITO-coated glass slides (50 \times 7 \times 0.7 mm, $R_s < 100 \Omega$) were purchased from Delta Technologies (part no. CG-90IN-CUV). The ITO-coated surface was first covered with ZnO NPs (Nanograde, ~50 nm diameter) to avoid quenching of NC emission by fast charge/energy transfer to the ITO. The ZnO NP layer (~60 nm thick, measured using a Dektak profilometer) was deposited by dip-coating the glass/ITO substrate into an ethanol suspension of ZnO NPs (2 mg ml⁻¹, one dip for 10 s) and annealed at 150 °C for 10 min in a nitrogen glovebox. To test the stability of the glass/ITO/ZnO NP substrates during potential scans, we performed control experiments in which we monitored changes in optical absorption spectra for prolonged exposures to negative and positive potentials. The results of these measurements indicate that the substrates are unaffected by either positive or negative EC potentials for exposure times of tens of minutes, which are much longer than the measurement time used in our SEC experiments (~10 min). The NCs were deposited onto the ZnO NP layer as a few-monolayer-thick film by dip-coating from a dilute toluene solution (optical density of 0.07 at 500 nm; two dips for 10 s). The ZnO NP layer used in this study was not treated with crosslinkers and therefore it represented a dielectric tunneling barrier of ~1 V. The introduction of the additional ZnO spacer as well as the presence of insulating surface ligands

can also lead to an appreciable attenuation of the actual shift of the FL compared to the nominal applied EC potential. The ITO was connected as a working electrode to the potentiostat (Bio Logic SP-200 Research grade potentiostat/galvanostat) and the film was placed into a quartz cuvette filled with the electrolyte (0.1 M tetrabutylammonium perchlorate (TBAClO₄) in propylene carbonate). Ag and Pt wires were used as quasi-reference and counter electrodes, respectively. All potentials reported in this work were measured relative to the quasi-reference Ag electrode during staircase voltammetry scans (10 s scan rate). The film was excited at 3.1 eV with continuous-wave diode lasers and the emitted light was collected with a focusing lens and sent to a spectrometer coupled to a TM-C10083CA Hamamatsu Mini-Spectrometer.

Magnetic Characterization

We used standard MCD methods⁶ to measure the field- and temperature-dependent Zeeman splitting (ΔE_Z) of the 1S exciton absorption resonance in our NCs, from which the presence of any additional *sp-d* exchange coupling of the exciton to paramagnetic dopants can be inferred. As in conventional diluted magnetic semiconductors⁷, paramagnetic moments in the NC are revealed via an enhanced and strongly temperature-dependent ΔE_Z . MCD measures, as a function of photon energy, the (normalized) difference in transmission between right and left circularly polarized light through the NC film in the Faraday geometry, $(T_R - T_L)/(T_R + T_L)$ ⁸. When the Zeeman splitting is small compared to the width of the 1S exciton absorption (as is the case here), the MCD spectrum is therefore derivative-like with a low-energy maximum proportional to ΔE_Z . NC films were mounted in the variable-temperature insert (1.5–300 K) of a 7 T superconducting magnet with direct optical access. Probe light of tunable wavelength was derived from a Xenon lamp directed through a spectrometer. The probe light was mechanically chopped at 137 Hz and was modulated between right and left circular polarizations at 50 kHz using a photoelastic modulator. The transmitted light was detected with a silicon avalanche photodiode. Photomagnetization was induced with additional light from a continuous-wave 3.05 eV diode laser.

Supporting Figure S1 – Au₇-GSH ESI-MS spectroscopy.

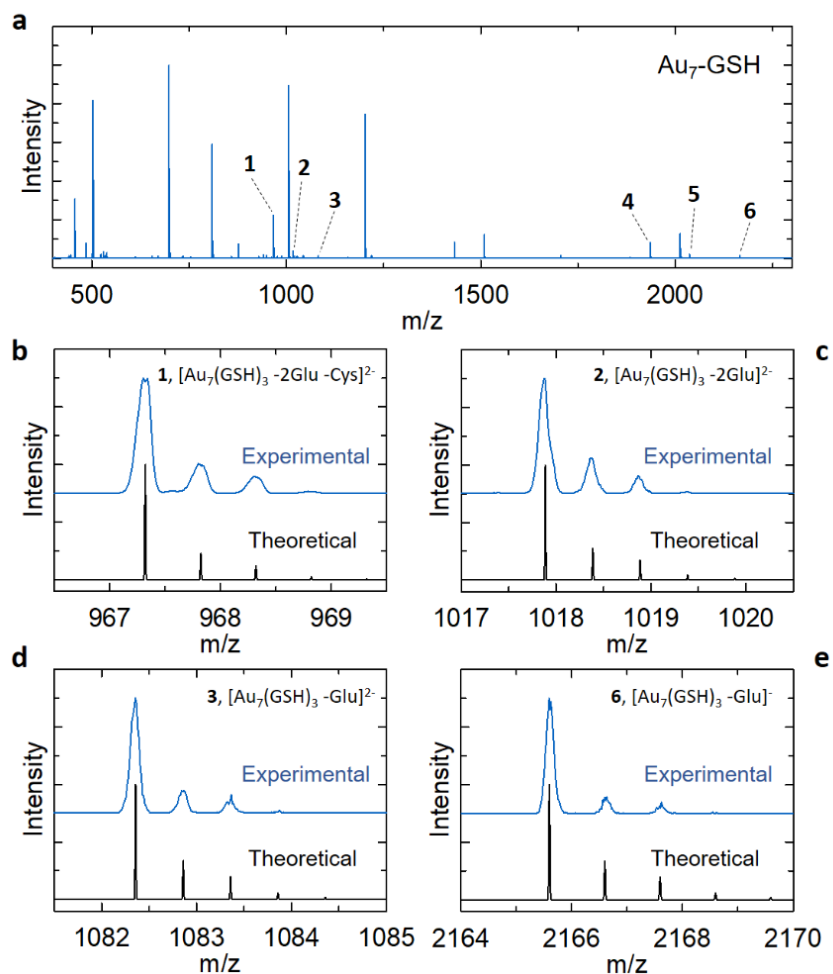


Figure S1 – (a) Positive mode ESI-MS spectra of gold clusters in aqueous solution. Experimental (blue) and simulated (black) isotopic patterns of m/z peaks n° 1 (b), 2 (c), 3 (d) and 6 (e) not enlightened in the main text (**Figure 1b**). The peaks are ascribed to gold clusters composed of seven Au atoms capped by three GSH ligands. The details on the peaks assignment are reported in Supporting **Table S1**.

Supporting Figure S2 - Optical absorption and PL spectra of Au:CdSe NCs synthesized at 170°C.

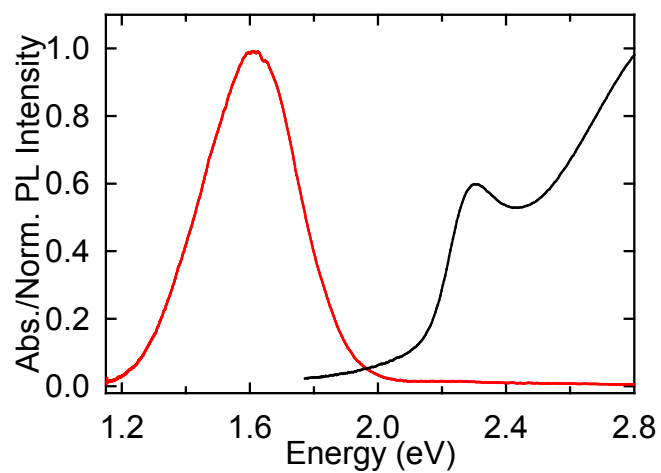


Figure S2 - Optical absorption (black line) and PL (red lines) spectra of Au:CdSe NCs produced with a reaction temperature of 170°C for 30 minutes.

Supporting Figure S3 – TEM Images and Size Analysis of Au-doped CdSe NCs with R=1.65 nm.

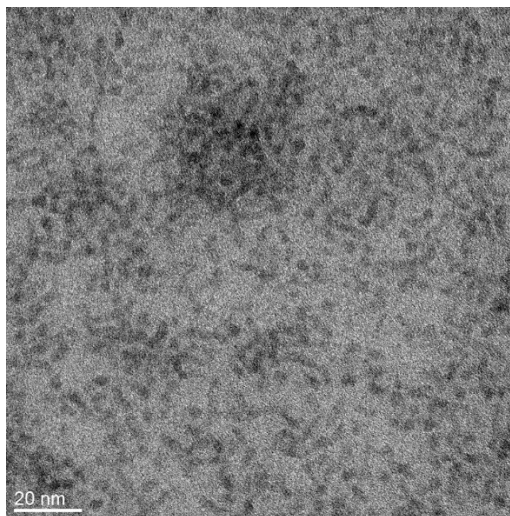


Figure S3 – Transmission electron microscopy (TEM) image of an ensemble of Au-doped CdSe NCs. The size analysis is reported in the main text (**Figure 1e**).

Supporting Figure S4 – Optical absorption and PL spectra of Au:CdSe NCs during their synthesis.

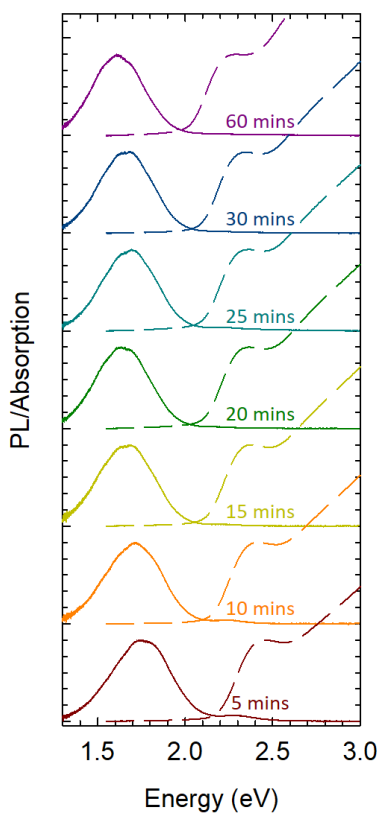


Figure S4 - Stacked optical absorption (dashed lines) and PL (continuous lines) spectra of various aliquots of Au:CdSe NCs during their synthesis.

Supporting Figure S5 – Reproducibility of the SEC response of Au:CdSe NCs under positive and negative EC potential.

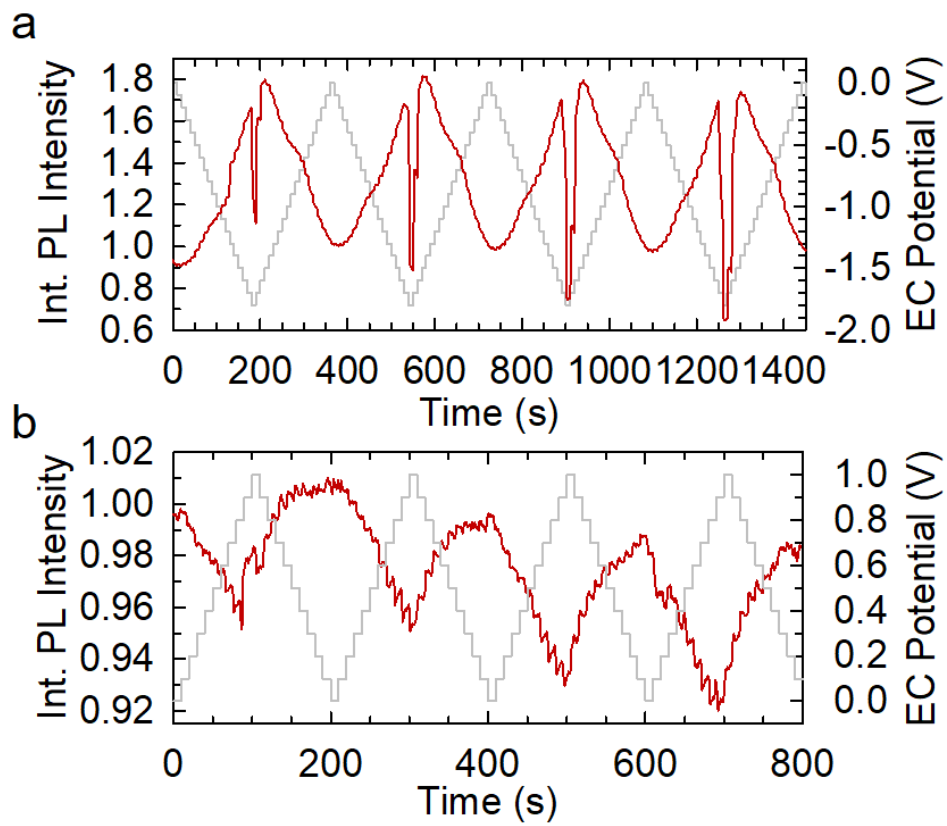


Figure S5 – Integrated PL intensity during four (a) negative and (b) positive EC cycles.

Supporting Figure S6– Au:CdSe NCs PL decay traces under negative EC potential.

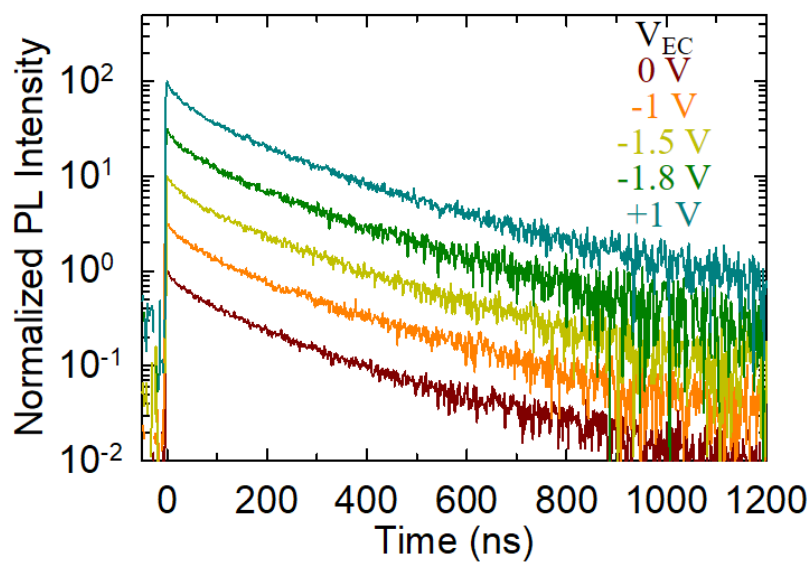


Figure S6 - Decay curves of the Au-PL of Au:CdSe NCs at different EC potentials. Excitation energy 3.1 eV.

Supporting Figure S7 – Energy shift of the 1S absorption peak and Au-related PL peak as a function of the reaction time.

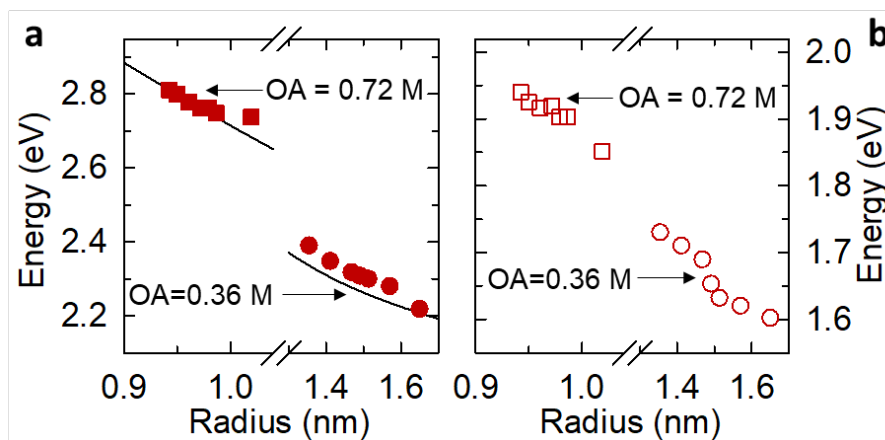


Figure S7 – Spectral positions of (a) the 1S absorption feature (filled symbols) and (b) the Au-related PL band (open symbols) as a function of particle radius for two sets of Au:CdSe NCs synthesized in the exact same conditions except for the amount of OA (squares for 0.72 M and circles for 0.36 M). The black line is the evolution of the band gap with the particle size extracted from reference 60.

Supporting Figure S8– TEM image and size analysis of Au:CdSe NCs with R=1.0.

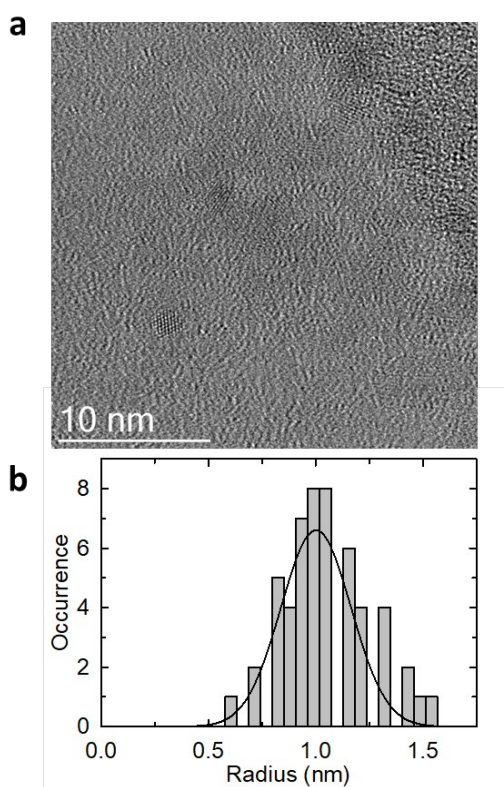


Figure S8 – TEM image and size analysis of Au:CdSe NCs. (a) TEM image of an ensemble of Au:CdSe NCs. (b) Statistical analysis of the size of 50 NCs from the TEM images. The average radius is 1.0 ± 0.1 nm (black line).

Supporting Figure S9 – TEM image and size analysis of Au:CdSe NCs with R=1.3.

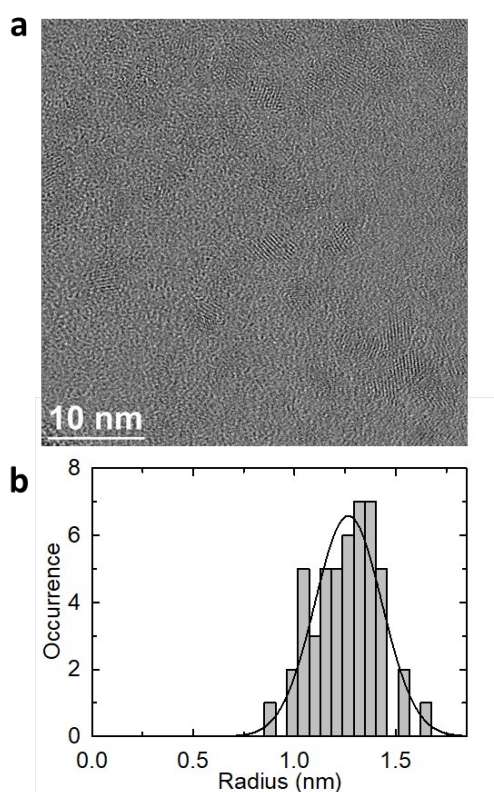


Figure S9– TEM image and size analysis of Au:CdSe NCs. (a) TEM image of an ensemble of Au:CdSe NCs. (b) Statistical analysis of the size of 50 NCs from the TEM images. The average radius is 1.3 ± 0.1 nm (black line).

Supporting Figure S10 - Optical absorption and PL spectra of Au: CdSe NCs during their synthesis with different concentrations of Au precursor.

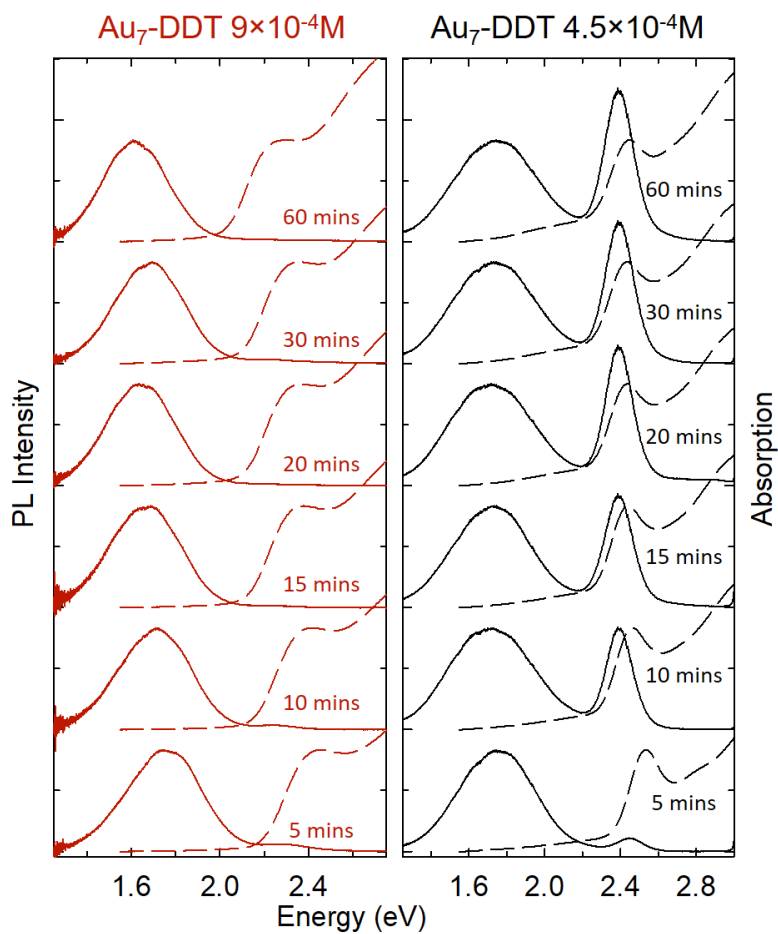


Figure S10 - Optical absorption (dashed lines) and PL (continuous lines) spectra of various aliquots of Au: CdSe NCs produced with different concentration of gold cluster 9×10^{-4} M (left panel) and 4.5×10^{-4} M (right panel). The condition with $[\text{Au}_7\text{-DDT}] = 9 \times 10^{-4}$ M refers to the synthesis of the NCs mainly discussed throughout the article and reported in Supporting **Figure S4**.

Supporting Figure S11 – Optical absorption and PL spectra of Au: CdSe NCs produced with Au acetate and Au(I) chloride as gold precursors.

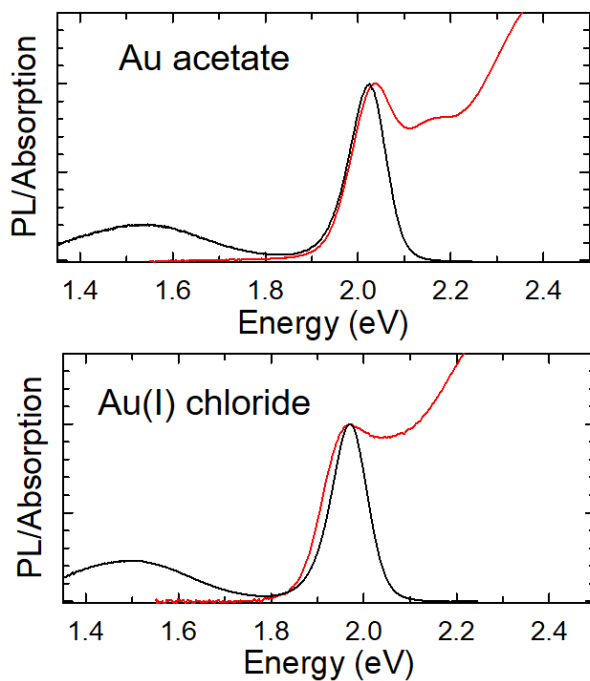


Figure S11 – Normalized optical absorption (red) and PL spectra (black) of Au: CdSe NCs doped synthesized used with Au acetate (upper panel) and Au(I) chloride (lower panel) as gold precursors in the reaction synthesis.

Supporting Figure S12 – Absorption spectra of Au:CdSe NCs during the etching process.

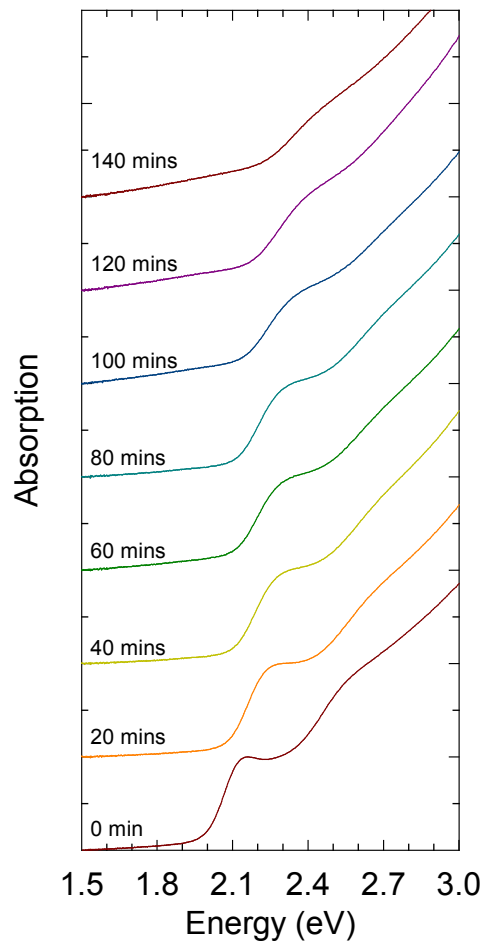


Figure S12 – Normalized optical absorption spectra of Au:CdSe NCs during the etching process. As expected, the absorption edge progressively shifts towards higher energies.

Supporting Figure S13 – TT maps of Au:CdSe NCs at increasing pump fluences.

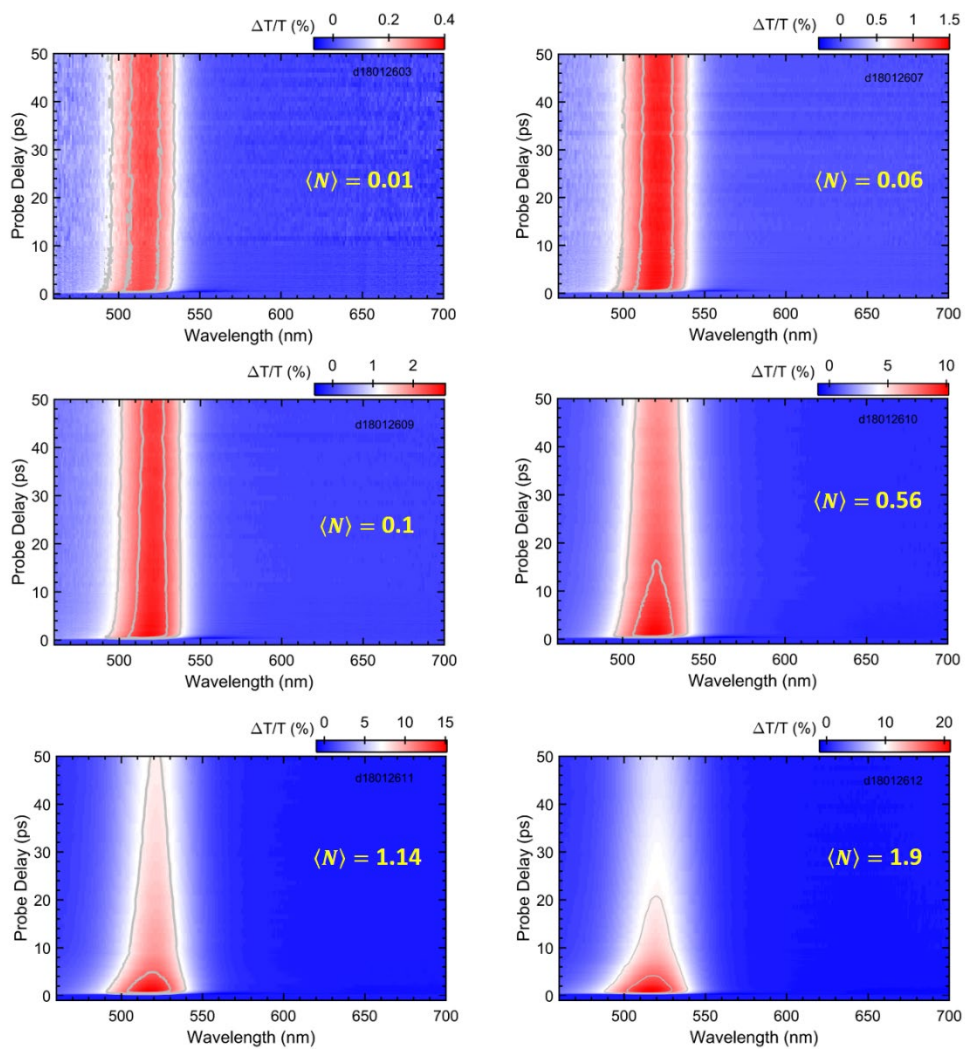


Figure S13 – TT contour plots of Au:CdSe NCs with R=1.1 nm as a function of increasing exciton occupancy. The grey lines correspond to $0.8 \times (\Delta T/T)_{\max}$ and $0.5 \times (\Delta T/T)_{\max}$.

Supporting Figure S14 – 1S bleaching dynamics of Au: CdSe NCs.

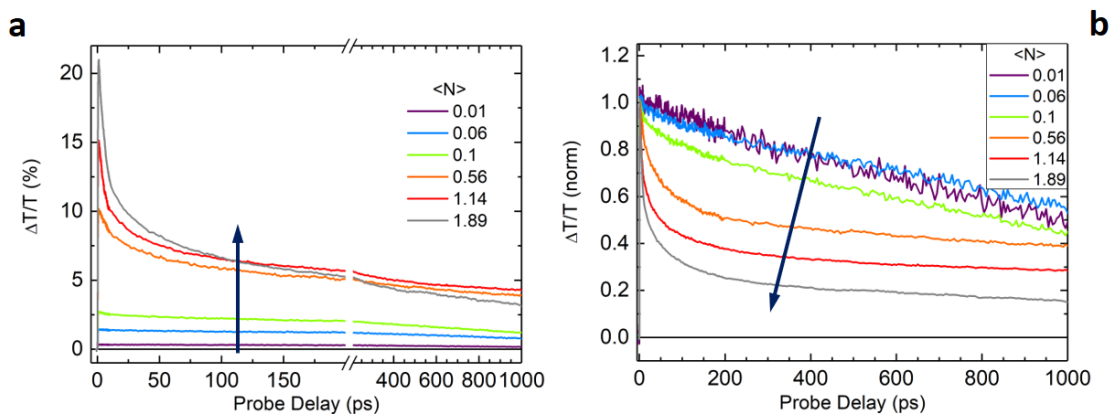


Figure S14 – (a) Photo-bleaching dynamics of Au: CdSe NCs at the 1S energy for increasingly higher pump fluence corresponding to the displayed average exciton occupancy $\langle N \rangle$. The progressive appearance of the fast component related is highlighted by normalizing the curves in panel a to their value at zero delay (b) and when the pump-probe delay is 600 ps

Supporting Figure S15 – Photoluminescence spectra of Au:CdSe NCs vs. excitation power in semi-logarithmic scale.

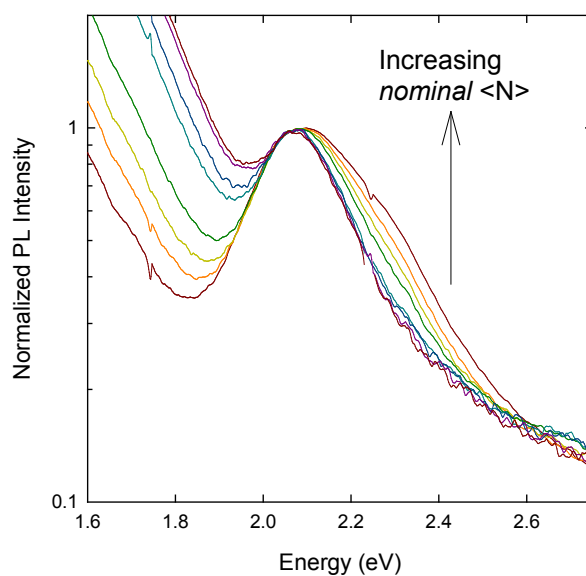


Figure S15 – Enlargement of the BE emission in the PL spectra of Au:CdSe NCs ($R=1.65$ nm) as a function of the nominal exciton population $\langle N \rangle$ ($E_{EX}=3.5$ eV, from $\langle N \rangle=0.7$ to $\langle N \rangle=60$ as indicated by the arrow), showing the emergence of a biexcitonic high-energy spectral component for *nominal* $\langle N \rangle$ -values above 10 excitons per NCs.

Supporting Figure S16 – Schematics of the experimental setup used for MCD measurements under additional UV excitation.

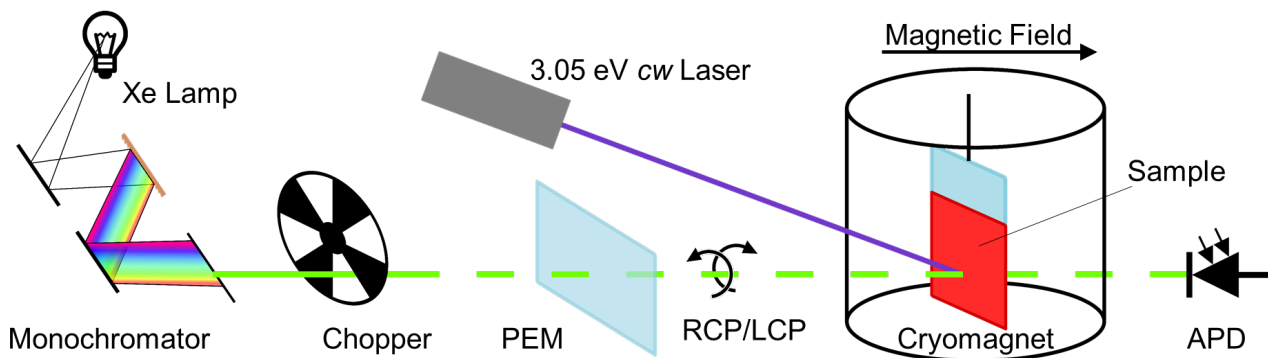


Figure S16 – Schematics of the experimental setup used for MCD measurements under additional UV excitation. The probe beam is produced by a Xe lamp coupled to a scanning monochromator. The beam is chopped with a mechanical chopper and its circular polarization is modulated between right and left circularly polarized using a photo-elastic modulator (PEM). The light transmitted through the sample, which is positioned in the variable temperature insert of a 7T magnet with direct optical access, is collected by an avalanche photodiode (APD). The additional UV light is provided by a CW laser at 3.05 eV incident onto the same position of the sample as the weak probe beam.

Supporting Table S1 - ESI-MS data analysis of the Au₇-GSH clusters

Table S1 reports the ESI-MS data analysis for the synthesized Au clusters capped with GSH molecules. We report the formula of the chemical species observed in the Au clusters mass spectrum measurements reported in **Figure 1b** and **Figure S1**, together with the experimental and simulated *m/z* values. **Figure S1** shows the comparison between experimental and simulated isotopic patterns for the peaks 1, 2, 3, 6 not enlightened in the main text.

Peak	Chemical species	Theoretical average <i>m/z</i> (Da)	Experimental average <i>m/z</i> (Da)
1	[Au ₇ (GSH) ₃ -2Glu-Cys] ²⁻	968.2	968.3
2	[Au ₇ (GSH) ₃ -2Glu] ²⁻	1018.8	1019.4
3	[Au ₇ (GSH) ₃ -Glu] ²⁻	1083.4	1083.9
4	[Au ₇ (GSH) ₃ -2Glu-Cys] ⁻	1936.4	1936.0
5	[Au ₇ (GSH) ₃ -2Glu] ⁻	2037.7	2038.9
6	[Au ₇ (GSH) ₃ -Glu] ⁻	2166.6	2167.9

Table S1 - Peak assignment for the ESI-MS measurement of Au clusters in water reported in Supporting **Figure S1** where Glu and Cys are, respectively, the glutamine and cysteine groups of the GSH molecules.

Supporting Table S2 – ICP-AES data of Au:CdSe NCs

	R [nm]		
	0.95	1.35	1.65
Au [at%]	5.53	1.47	0.8
Cd [at%]	68.32	63.49	55.7
Se [at%]	26.15	35.04	43.6

Table S2 – Atomic percentage of gold, cadmium and selenium as obtained from ICP-AES analysis of Au:CdSe NCs with radius R.

Supporting Table S3 – Average number of excitons generated per unit time using cw 3.05 eV illumination in the photo-assisted MCD experiment.

	Power [μW]	$\langle N \rangle$
I_0	0.3	0.047
$3.65 * I_0$	1	0.171
$10 * I_0$	3	0.466
$36.5 * I_0$	10	1.71
$100 * I_0$	30	4.66

Table S3 - Average number of excitons generated per unit time using cw 3.05 eV illumination in the photo-assisted MCD experiment.

In the model described by Eq. (2), since the localization efficiency of valence band holes in Au^+ is 100%, the term $\langle N \rangle$ corresponds to the number of Au^{2+} states per nanocrystal generated in one second of continuous illumination. The equilibrium Au^{2+} population per nanocrystal, accounting for the MCD signal, is determined by the respective time kinetics discussed in the main text.

Supporting Discussion - Quantification of the Au/NC ratio

First, we calculate the volume of the single NC in spherical particle approximation (using data from TEM analysis reported in **Figure 1e**):

$$V_{\text{NC}} = 4/3 \times \pi \times R^3 = 4/3 \times \pi \times 1.65^3 = 19 \pm 7 \text{ nm}^3$$

Then, we calculate the volume of the unit cell of CdSe in cubic, ZB structure (as shown by XRD data reported in **Figure 1f**, lattice constant of bulk ZB CdSe is $a = 0.608 \pm 0.001 \text{ nm}^9$):

$$V_{\text{cell}} = a^3 = 0.608^3 = 0.22 \pm 0.01 \text{ nm}^3$$

We can therefore obtain the total number of unit cell per NC

$$N_{\text{cell}} = V_{\text{NC}} / V_{\text{cell}} = 19 / 0.22 = 86 \pm 32$$

and the total number of atoms

$$A_{\text{QD}} = N_{\text{cell}} \times A_{\text{cell}} = 86.4 \times 8 = 691 \pm 246$$

Considering the percentage of Au atoms obtained by ICP-AES data reported in Supporting **Table S2** (at% Au = 0.8%), we obtain that

$$\text{Atoms of Au per NC} = 6 \pm 2$$

The same procedure is performed for $R=0.9 \text{ nm}$ and $R=1.35 \text{ nm}$ using the respective Au at%.

Supporting References

1. Luo, Z.; Yuan, X.; Yu, Y.; Zhang, Q.; Leong, D. T.; Lee, J. Y.; Xie, J. *J. Am. Chem. Soc.* **2012**, 134, (40), 16662-70.
2. Yang, Y. A.; Wu, H.; Williams, K. R.; Cao, Y. C. *Angew. Chem.* **2005**, 117, (41), 6870-6873.
3. Siy, J. T.; Bartl, M. H. *Chem. Mater.* **2010**, 22, (21), 5973-5982.
4. Wills, A. W.; Kang, M. S.; Wentz, K. M.; Hayes, S. E.; Sahu, A.; Gladfelter, W. L.; Norris, D. *J. J. Mater. Chem.* **2012**, 22, (13), 6335.
5. Yergey, J. A. *Int. J. Mass Spectrom. Ion Phys.* **1983**, 52, (2), 337-349.
6. Kuno, M.; Nirmal, M.; Bawendi, M. G.; Efros, A.; Rosen, M. *J. Chem. Phys.* **1998**, 108, (10), 4242-4247.
7. Furdyna, J. K. *J. Appl. Phys.* **1988**, 64, (4), R29-R64.
8. Bussian, D. A.; Crooker, S. A.; Yin, M.; Brynda, M.; Efros, A. L.; Klimov, V. I. *Nat. Mater.* **2009**, 8, (1), 35-40.
9. West, A. R., *Solid State Chemistry and Its Applications*. 2012.